STRUCTURAL ANALYSIS OF BONAIRE, NETHERLANDS LEEWARD

ANTILLES-A SEISMIC INVESTIGATION

A Thesis

by

JACOB BARTSCHT BAYER

Submitted to the Office of Graduate and Professional Studies of
Texas A&M University
in partial fulfillment of the requirements for the degree of

MASTER OF SCIENCE

Chair of Committee,	Bobby Reece
Committee Members,	Juan Carlos Laya
	Carlos Alvarez Zarikian
Head of Department,	Mike Pope

August 2016

Major Subject: Geophysics

ABSTRACT

We show that the island of Bonaire, Netherlands Antilles exhibits strain indicative of local deformational processes and regional tectonics. We acquired ~172 km of 2D multichannel seismic reflection profiles in the nearshore environment on the west side of Bonaire to evaluate the geology for structural deformation. By integration of previous geological and geophysical studies with our data, we ascertained what tectonic stress and local processes affect the island of Bonaire. Our analysis reveals: 1) a large anticline that extends from onshore the north of Bonaire to at least ~17 km offshore, and is the result of regional Pliocene-Quaternary compression; 2) a feature in the seafloor off the SW coast of Bonaire that is either the result of antecedent topography or late Paleogene NW-SE-directed compression; 3) a rotational slump of the seafloor due to either uplift of the entire island or subsidence of the south of the island; 4) NW-SE-striking faults related to a present regional NE-SW-directed extension, which indicates that footwall uplift of reactivated normal faults is the mechanism for recent uplift of the ABCs. This study highlights the utility of a localized inexpensive high-resolution seismic study to fill in knowledge gaps and further constrain the tectonics of the Caribbean-South American plate interaction. Additionally, this study shows what factors potentially influence material failure on unsedimented hard rock marine slopes. Finally, understanding what deformation is present on Bonaire and what stresses are imparting the observed strain, can serve as an aid to the inhabitants of the island to mitigate risk.

DEDICATION

To my wife and family

ACKNOWLEDGEMENTS

NOMENCLATURE

ABCs   Netherlands Leeward Antilles: Aruba, Bonaire, Curaçao

SCDB   South Caribbean Deformed Belt

TWT   Two-Way-Travel Time

CMP   Common Mid Point

TABLE OF CONTENTS

LIST OF FIGURES

Page

LIST OF TABLES

1. INTRODUCTION

The geology of offshore basins in the southern Caribbean provide a record of Caribbean-South American plate interaction (Gorney et al., 2007). Since this record lies beneath the Caribbean Sea, the onshore geology of the Leeward Antilles has been investigated by numerous workers over the years for insight into the complex Caribbean-South American Plate interaction (Fig.1).

Bonaire, an island in the Leeward Antilles, is located approximately 90 km offshore northwestern Venezuela (Fig. 1). The igneous basement of Bonaire originated during the Cretaceous in the Pacific Ocean on the former leading edge of the Caribbean plate and has moved eastward since its formation (Beets et al., 1977; Thompson et al., 2004; Hippolyte and Mann, 2011; Wright and Wyld, 2011). During the Pliocene-Quaternary, Bonaire was elevated above sea level allowing for the for the growth of carbonates in the Pleistocene on the submerged portions of the island (Hippolyte and Mann, 2011). Since the Pleistocene, the island of Bonaire has experienced glacio-eustatic sea level fluctuations and tectonic uplift, which is recorded in the onshore Pleistocene carbonate terraces (Alexander, 1961; Hippolyte and Mann, 2011).

Previous studies have analyzed the onshore geology of Bonaire and the adjacent sedimentary basins for structural deformation. Beardsley and Avé Lallemant (2007) investigated the Cretaceous igneous basement of Bonaire and constrained three phases of deformation affecting the igneous basement from the early cretaceous to the late Paleogene. In the sedimentary basins adjacent to Bonaire, Gorney et al. (2007)

1

conducted a geophysical structural interpretation and classified three phases of faulting: 1) E-W-striking Eocene-Oligocene normal faults; 2) NW-SE-striking Oligocene-Holocene normal faults; 3) WNW-ESE-striking middle Miocene-Holocene reverse faults. Hippolyte and Mann (2011) analyzed the Neogene-Quaternary geology of Bonaire and while they were unable to find evidence of deformation in the Quaternary geology of the island, the Pleistocene carbonate terraces, they were able to constrain three phases of deformation affecting the island: 1) NW-SE-directed late Paleogene; 2) NNW-SSE and NNE-SSW-directed middle Miocene syndepositional extension; 3) NNE-SSW-directed Pliocene-Quaternary compression. While past workers provide insight into the regional and local tectonics of Bonaire, the present day stress on Bonaire and across the region is not well constrained.

This study uses an integration of 2D marine seismic reflection data acquired nearshore, off the west coast of Bonaire, and the previous structural studies to interpret strain on the island. The goal of this study is to determine what deformation is present in the submarine nearshore environment and what stresses, are imparting the observed strain. This tectonic analysis of Bonaire helps to constrain the local processes and regional tectonics imparting stress on the island and provides new insights into the Caribbean-South American tectonic environment.

1.1 Background

1.1.1 Location and Plate Motion of Study Area

The island of Bonaire is located approximately 90 km offshore northwestern Venezuela in the Leeward Antilles islands, which are comprised of the Netherlands Leeward Antilles in the west and the islands of the Federal Dependencies of Venezuela in the east. The Netherlands Leeward Antilles, also known as the Dutch Leeward Antilles, include the islands, from west to east, Aruba, Curaçao, and Bonaire (Fig. 1). Collectively, the Netherlands Leeward Antilles are often referred to as the 'ABCs.'

The ABCs are located in the plate boundary zone between the Caribbean and South American plates termed the 'Bonaire Block' (Fig. 1) (Silver et al., 1975). Authors have described the Bonaire Block as a distinct structural block that has fragmented from the interaction of the South American and Caribbean plates since the Cretaceous (Silver et al., 1975; Van der Lelij et al., 2010; Boschman et al., 2014; Keppie, 2014). The South Caribbean Deformed Belt (SCDB), an accretionary wedge resulting from the subduction of the Caribbean plate at a shallow angle beneath the South American plate since the middle Eocene, defines the western and northern edges of the Bonaire Block (Kellogg, 1984; Colmenares and Zoback, 2003; Escalona and Mann, 2011; Kroehler et al., 2011; Escalona and Yang, 2013). To the south, the right-lateral strike-slip faults of the Oca-Ancón and San Sabastian fault zones bound the Bonaire Block (Audemard, 2001). In the east, the Los Roques Canyon delineates the Bonaire Block (Fig. 1).

Presently the Bonaire and Maracaibo Blocks are being extruded to the N-NE because of the collision and suturing of the Panama Block to the Pacific side of northern South America (Fig. 2) (Audemard et al., 2005). This N-NE extrusion drives the convergence of the Bonaire Block and the Caribbean plate at the SCDB, where the Bonaire Block overrides the shallow subducting Caribbean plate (Audemard et al., 2005). GPS measurements from Kaniuth et al. (1998) and Trenkamp et al. (2002) support the N-NE escape of these blocks, while the GPS measurements of Pérez et al. (2001) indicate that the Bonaire block is also moving to the east.

Currently, the Caribbean plate is moving east relative to the surrounding North and South American plates at an average rate of 20 mm yr^{-1} (DeMets et al., 2000; Weber et al., 2001; Trenkamp et al., 2002). The ABCs are also moving to the east, but at a slower rate of 13-17 mm yr^{-1} relative to South America (Pérez et al., 2001). This differential motion between the ABCs and the Caribbean plate supports the interpretation that the ABCs are accreting onto the South American plate (Escalona and Mann, 2011; Escalona and Yang, 2013). North of the ABCs, Symithe et al. (2015) modeled the N-S convergence responsible for the underthrusting of the Caribbean plate at the SCDB at a rate of 3-8 mm yr^{-1}.

1.1.2 Geologic Provenance

Over the years, authors have debated the origin of the Caribbean plate, however, the general consensus among modern literature is that the Caribbean plate formed in the

Pacific Ocean and has moved eastward since the Cretaceous (Van der Lelij et al., 2010; Escalona and Mann, 2011; Neill et al., 2011; Wright and Wyld, 2011; Boschman et al., 2014; Spikings et al., 2015; Whattam and Stern, 2015).

The Cretaceous basement rocks of the ABCs, Aves Ridge, and Greater Antilles have been interpreted as remnants of a continuous and single 'Great Arc of the Caribbean' on the former leading edge of the Caribbean plate (Fig. 3) (Beets et al., 1984; Burke, 1988; Gorney et al., 2007; Escalona and Mann, 2011; Hippolyte and Mann, 2011; Pindell et al., 2012; Boschman et al., 2014). Thompson et al. (2004) and Wright and Wyld (2011) differentiated the basement of Bonaire from that of Aruba and Curaçao; they interpreted Bonaire as part of the Great Arc of the Caribbean and Aruba and Curaçao as fragments of the younger Pacific-derived oceanic plateau that constitutes the Caribbean plate. Neill et al. (2011) interpreted Bonaire to derive from a separate smaller arc rather than a single Great Arc of the Caribbean, and showed the basement of the Aves Ridge to be geochemically unrelated to the ABCs and Greater Antilles (Fig. 4).

1.1.3 Tectonic Setting of the Netherlands Leeward Antilles

Post-Cretaceous tectonic structures have been interpreted in the region around the ABCs (Fig. 5). During the late Eocene-early Oligocene the Bonaire and Falcón basins opened up along east-west-striking normal faults due to N-S extension (Beardsley and Avé Lallemant, 2007; Bezada et al., 2008). A second phase of rifting followed during the late Oligocene-early Miocene forming northwest-southeast-striking normal

faults that bound the basement highs and adjacent basins of the ABCs (Beardsley and

Avé Lallemant, 2007; Gorney et al., 2007). Based on observations of current seafloor

offsets along these Oligocene-early Miocene normal faults, Gorney et al. (2007)

interpreted the second phase of extension as remaining active to the present. Since the

middle Miocence, uplift and inversion of the Falcón basin has occurred, while thermal

subsidence has resulted in the deepening of the Bonaire basin (Biju-Duval et al., 1982;

Porras, 2000; Gorney et al., 2007). This inversion of the Falcón basin resulted in a E-NE

trending fold-and-thrust belt that can be traced over 200 km across the basin (Fig. 5).

Located offshore to the northeast of the Falcón basin is the 175-km-long La Vela fold-

thrust belt that displays NE-SW shortening (Fig. 5) (Gorney et al., 2007). The La Vela

fold-thrust belt has been interpreted as either the product of gravity-induced sliding from

nearby onshore Venezuela into deeper water as the result of the combined uplift and

inversion of the Falcón basin (Porras, 2000; Gorney et al., 2007), or shortening related to

the N-NE escape of the Maracaibo Block (Hippolyte and Mann, 2011). Presently, N-S

shortening occurs at the SCDB, resulting in the E-W trending reverse faults to the north

of the ABCs (Fig. 5) (Gorney et al., 2007; Kroehler et al., 2011).

Utilizing marine seismic data as well as onshore geologic data collected by

preceding workers, Gorney et al. (2007) mapped the aforementioned tectonic events in

the offshore basins around the ABCs, and constrained these events into three 'fault

families' as termed by Hippolyte and Mann (2011) (Fig. 5):

1. E-W-striking Eocene-Oligocene normal faults

2. NW-SE-striking Oligocene-Holocene normal faults

6

3. WNW-ESE-striking middle Miocene-Holocene reverse faults

Hippolyte and Mann (2011) correlated the fault families of Gorney et al. (2007) with kinematics of faults and tectonic structures interpreted on the surface Neogene-Quaternary geology of the ABCs, and classified the interpreted deformation into three regional tectonic phases:

1. NW-SE-directed late Paleogene compression

2. NNW-SSE and NNE-SSW-directed middle Miocene syndepositional extension

3. NNE-SSW-directed Pliocene-Quaternary compression responsible for the NW-SE trending anticlines interpreted on the ABCs

1.1.4 Regional Stress Affecting the Bonaire Block

The present day regional stress across the Bonaire Block and the ABCs is not well constrained. Schubert and Scheidegger (1986) interpreted that the present principal stress (σ_1) direction of the Curacaos is NNW-SSE compression based on 136 joint measurements in the Pleistocene carbonate terraces. This present principal stress (σ_1) interpreted by Schubert and Scheidegger (1986) aligns with the present NNW-SSE principal stress (σ_1) interpreted by Audemard et al. (2005) at the Oca-Ancón, San Sabastian, and El Pilar faults located to the south of ABCs. The interpretation of Schubert and Scheidegger (1986) approximately aligns with the present NE-SW-directed shortening occurring in the La Vela fold-thrust belt located ~30-100 km south of the ABCs. However, Hippolyte and Mann (2011) dismissed the interpretation of Schubert

and Scheidegger (1986), stating that joints do not necessarily reflect the trend of (σ_1), and argued instead that joints generally only indicate direction of the minimum principal stress axis (σ_3). Hippolyte and Mann (2011) along with Audemard et al. (2005) interpreted that the GPS movements from Pérez et al. (2001) and Weber et al. (2001) indicated that the current regional tectonic regime affecting the Bonaire Block is extension and/or transtension. It should be noted that these GPS measurements from Pérez et al. (2001) and Weber et al. (2001) are not robust in the area of the Bonaire Block due to the limited number of GPS sites.

The present day deformation of the ABCs and the Bonaire Block is hypothesized to be the result of two main factors (Silver et al., 1975; Hippolyte and Mann, 2011):

1. The N-NE movement of the Maracaibo block
2. The eastward movement of the Caribbean Plate relative to the South American plate

If the N-NE tectonic escape of the Maracaibo is still active and regionally dominant, then NNE-SSW compression could possibly occur in the Bonaire Block and the ABCs (Hippolyte and Mann, 2011). If the N-NE tectonic escape of the Maracaibo is not active or slow, then the right lateral movement of the Caribbean plate is dominant and NE-SW extension and/or transtension could possibly occur (Hippolyte and Mann, 2011). The lack of robust field observations from previous workers in the Bonaire Block and the ABCs makes constraining the prevalence of these two aforementioned scenarios difficult.

To date no faults have been interpreted in the exposed quaternary geology on the ABCs (Hippolyte and Mann, 2011). In the adjacent basins offshore the ABCs, recent seafloor offsets along the Neogene faults (Gorney et al., 2007) indicate a present NE-SW extensional tectonic regime (Hippolyte and Mann, 2011). However, Audemard et al. (2005) interpreted recent GPS measurements from Kaniuth et al. (1998) and Trenkamp et al. (2002) to support the fact that both the Maracaibo and Bonaire Blocks are presently tectonically escaping to the N-NE. This interpretation from Audemard et al. (2005) supports the notion that compression would be the dominant stress affecting the Bonaire Block. On the other hand, as stated earlier, Audemard et al. (2005) along with Hippolyte and Mann (2011), interpreted that the GPS measurements from Pérez et al. (2001) and Weber et al. (2001), though not robust, indicated that some magnitude of extension and/or transtension affects the Bonaire Block and the ABCs.

1.1.5 Stratigraphy of Bonaire

The basement geology of Bonaire has been conventionally mapped as a single stratigraphic section named the Washikemba Formation, and described as consisting of Cretaceous sedimentary, volcanoclastic, and intrusive rocks (Fig. 6) (Pijpers, 1933; Klaver, 1976; Beets et al., 1977; Beets et al., 1984; Priem et al., 1986; Jackson and Robinson, 1994; Thompson et al., 2004; Van der Lelij et al., 2010). However, Wright and Wyld (2011) mapped the basement geology of Bonaire as two unrelated stratigraphic units, the Washikemba Group and the Matjis Group, separated by a

transstensional fault named the 'Bartol Fault' (Fig. 7). The Washikemba Group and the

Matjis Group partially overlap in age, with the Matjis Group containing the oldest and

youngest rock ages. Though the sense of offset along the Bartol fault has yet to be

determined, the Matjis Group has been mapped on the northeast side of the fault, while

the Washikemba Group has been mapped on the southwest side of the fault (Wright and

Wyld, 2011). The Matjis Group is unconformably overlain by the middle-to-late

Campanian limestone Rincon Formation (Van der Lelij et al., 2010; Wright and Wyld,

2011). Unconformably overlying the Rincon formation is the Eocene Soebi Blanco

Formation, a conglomerate with clast derived from the underlying geology on Bonaire as

well as clasts from continental northern South America (Zapata et al., 2014). The Soebi

Blanco Formation is unconformably overlain by Eocene limestones, which are

unconformably overlain by the steeply dipping limestone beds of the Miocene-Pliocence

Seroe Domi Formation (Beets et al., 1977). Approximately 165 m of Pleistocene

carbonate terraces unconforambly overlie the Seroe Domi Formation (Fig. 6) (Sulaica,

2015).

1.1.6 Pleistocene Carbonate Terraces

Previous authors identified and classified four Pleistocene carbonate terraces on

Bonaire and across the ABCs (Sulaica, 2015). The elevated and terraced reefs of Bonaire

and the ABCs are indicative of reef formation during slow tectonic uplift along active

margins, like the terraced reefs of Barbados (Muhs et al., 2012). Herweijer and Focke

10

(1978), Schellmann et al. (2004), and Muhs et al. (2012) dated the approximate age of the first terrace to 125 ka, which is similar to the 129 ka age approximation by Schubert and Szabo (1978) . Herweijer and Focke (1978) and Schubert and Szabo (1978) estimated the date of the second terrace to ~500 ka, while Sulaica (2015) estimated the date of the second terrace to ~200-220 ka. Sulaica (2015) estimated the ages of the third and fourth terrace to ~330 ka and ~405 ka respectively. The age constraints of the second-fourth terraces are tenuous interpretations as no geochemical dating of these terraces has occurred (Sulaica, 2015). The Pleistocene carbonate terraces are proposed to have grown during both eustatic sea level rise and tectonic uplift (Baker, 1924; Alexander, 1961; De Buisonjé, 1974; Herweijer and Focke, 1978; Sulaica, 2015). The only estimates for tectonic uplift rates of the Pleistocene carbonate terraces come from Herweijer and Focke (1978). Herweijer and Focke (1978) calculated that the second terrace uplifted at an average rate of 0.05 m/1000 years for the last 500 ka, based on their estimated age of the second terrace at ~500 ka. Additionally, Herweijer and Focke (1978) calculated that the first terrace uplifted at an average rate of 0.04 m/1000 years for the last 125 ka, based on their estimated age of the first terrace of ~125 ka. The mechanism for tectonic uplift of the Pleistocene carbonate terraces has been attributed to folding based on the 5° tilt of the terraces (De Buisonjé, 1974), while more recently Hippolyte and Mann (2011) attributted the uplift to footwall uplift via reactivation of the normal faults, fault family 2, that bound the basement highs of the ABCs.

1.1.7 Seroe Domi Formation

       The Miocence-Pliocene Seroe Domi Formation is a steeply dipping limestone formation found only in the northern part of the island (Fig. 6). Researchers have conventionally mapped the Seroe Domi formation extending from the northern portion of Bonaire to the central portion of the island (Bandoian and Murray, 1974; De Buisonjé, 1974; Hippolyte and Mann, 2011), but a more recent assessment reduced the distribution to a small area only in the northern part of the island (Sulaica, 2015). The more recent assessment by Sulaica (2015) suggests that the Seroe Domi Formation continues along strike below the subsurface.

       The inclined beds of the Seroe Domi Formation range in dip from 28°-38° (Bandoian and Murray, 1974; Hippolyte and Mann, 2011; Sulaica, 2015). The origin of the high-angle dips of the Seroe Domi Formation has long been debated; and two interpretations regarding the cause of the steep dips prevail among authors:

1. The dips of the Seroe Domi Formation are syndepositional and the limestones were deposited in the present inclined position on the sloping antecedent topography (Deffeyes et al., 1965; Bandoian and Murray, 1974; De Buisonjé, 1974; Herweijer et al., 1977).

2. The dips of the Seroe Domi Formation are secondary, and are the result of tectonic folding and compression after deposition (Pijpers, 1933; Hippolyte and Mann, 2011)

1.1.8 Anticlines on Bonaire and the Netherlands Leeward Antilles

Previous authors have interpreted an anticline to exist on Bonaire (Baker, 1924; Pijpers, 1933; Silver et al., 1975; Hippolyte and Mann, 2011). Baker (1924) first proposed that the island of Bonaire is superficially an anticline and noted that the axis of the anticline extends NW-SE. Pijpers (1933) resolved that the Cretaceous geology exposed on the northern part of the island is the northeast limb of NW-SE trending anticline. Silver et al. (1975) mapped offshore an anticline axis trending NW-SE, based on data from Silver et al. (1972) but did not comment on it (Fig. 8). To explain the tilting of the Miocene-Pliocene Seroe Domi Formation, Hippolyte and Mann (2011) proposed that the most elevated area of Bonaire represents the crest of a broad anticline and interpreted the anticline as trending NW-SE based on dip measurements from De Buisonjé (1974) (Fig. 6).

Baker (1924), Silver et al. (1975), and Hippolyte and Mann (2011) all interpreted the existence of anticlines on Aruba and Curaçao as well. Hippolyte and Mann (2011) interpreted that the anticlinal folds of the ABCs, as with Bonaire, date to after the deposition of the Miocene-Pliocene Seroe Domi Formation in order to account for the 28-38° dip of the Seroe Domi Formation. Hippolyte and Mann (2011) constrained this folding to the Pliocene-Quaternary; and interpreted the cessation of this NNE-SSW compression to sometime in the Quaternary based on recent GPS measurements (Pérez et al., 2001) that indicate the present regional tectonic regime is extension. Additionally,

13

Hippolyte and Mann (2011) attributed the compression responsible for the NW-SE trending anticlines to also be the mechanism that elevated the ABCs above sea level.

1.1.9 Nearshore Characterization of the Seafloor off the West Coast of Bonaire

Numerous researcher over the years have studied the geology, morphology, sedimentation, and biology in the shallow waters along the leeward coast of Bonaire. Hall (1999) studied the geomorphological evolution of the slopes and sediment chutes on forereefs along the leeward coast of Bonaire. The majority of research carried out by Hall (1999) occurred at dive sites in water depths up to ~40 m in the north region we refer to in this paper. In this nearshore study, Hall (1999) observed fringing reefs that lacked well-developed back-reef lagoons and slide scarps from reef structure failure that act as chutes and channels for a constant flow of sediment. Hall (1999) noted that the side exposure along the scarps and sediment channels consisted of an average of ~2 m of cemented limestone.

The majority of the nearshore observations of Bak (1977), Van Duyl (1985), and Keller (2011) occur in the central and south regions we refer to in this paper. Like Hall (1999) observed in the north, Bak (1977) and Van Duyl (1985) observed that sediment accumulation and transport occurs within grooves in the shallow living reefs. Van Duyl (1985) and Keller (2011) observed that the modern reefs grow on and around exposed fossilized reefs and limestone substrates. Keller (2011) and Bak (1977) observed that the

most prolific fringing reef growth occurs at ~10-50 m below sea level, however they noted that some living reef colonies exist at depths up to ~100 m.

During submarine dives exploring sponge diversity in deep water off the southern coast of Bonaire, researchers observed long stretches of fossilized reefs and collected limestone rocks at depths from ~90-250 m (Fig. 9 and Fig. 10) (Soest et al., 2014). This observation aligns with the proposed interpretation of Sulaica (2015) that maps the Pleistocene limestone terraces continuing offshore Bonaire (Fig. 11). At shallower depths, ~10-45 m, Soest et al. (2014) observed that the modern reefs were growing on limestone substrate; which aligns with the observations of previous authors that the modern reefs grow on top fossilized reefs. Soest et al. (2014) also observed a vast 'sand scape' surrounding the limestone substrates at depths from ~90-250 m, but did not make an observation about the lithologic composition of the sand scape.

The general consensus from previous researchers is that modern reef growth occurs most prolifically on exposed limestone substrates at depths up to ~40-50 m in all of the same regions we acquired seismic data (Bak, 1977; Van Duyl, 1985; Hall, 1999; Keller, 2011; Soest et al., 2014). Additionally, the general consensus among past workers is that sediment accumulation is not prolific along the leeward coast of Bonaire, and that most sediment accumulates and quickly flows basin-ward through nearshore grooves and channels (Van Duyl, 1985; Hall, 1999; Bales, 2016).

1.1.10 Estimated Velocity Values for Possible Seafloor Lithology of Bonaire

The geology of Bonaire predominately consists of Cenozoic carbonate successions on a Cretaceous igneous basement (Sulaica, 2015). Thompson et al. (2004) classified the exposed igneous basement on Bonaire consisting predominantly of felsic volcanoclastic rocks and basalt. Bales (2016) interpreted that the lithology of the seafloor off Bonaire could be comprised of either the: igneous basement, carbonate formations, or some magnitude of sediment.

Published velocity and density values of water saturated lithology similar to that of Bonaire can be used to estimate velocity and density values of the lithology comprising the seafloor of Bonaire. One of the constituent lithologies of the igneous basement of Bonaire is basalt, and Salisbury and Christensen (1978) calculated that saturated basalt from the seafloor at a mid-ocean ridge has an average P wave velocity of 5.9 (km/s) and an average density of 3.1 (g/cm^3) (Table 1). The other constituent lithology of the igneous basement of Bonaire is felsic volcanoclastic rocks, of which granite is the most common felsic rock. Barrett and Froggatt (1978), found that the average P wave velocity of saturated granite collected from the seafloor off Antarctica is 4.7 (km/s) and the average density is 2.7 (g/cm^3) (Table 1).

In regards to the values of possible limestone seafloor, Hamilton (1978) found that end member values of P wave velocities for saturated hard limestone are 3.2-5.5 (km/s) and that the end member density values are 2.7-2.3 (g/cm^3) (Table1).

A sediment based seafloor lithology is also considered based on the observations of Van Duyl (1985), Bruggemann (1995), Hall (1999), Soest et al. (2014), and Bales (2016). Offshore terrigenous sediment is minimal off the coast of Bonaire due to the semi-arid climate and lack of abundant rainfall (Bales, 2016). Bruggemann (1995), Hall (1999), and Perry et al. (2012) noted that the sediment off Bonaire consists predominately of calcareous sediment that results from biogenic production, bioerosion, and physical erosion of the living reefs and limestone rocks. To date, no detailed studies of the velocity and density of the sediment located offshore Bonaire exist. However, velocity and density studies of calcareous sediment offshore Hawaii do exist and can be used as an analogue to approximate these values for the sediment off Bonaire. Jackson and Richardson (2007) noted that the average P wave velocity of calcareous sediments collected off the coast of Hawaii ranged from ~1.6-1.8 (km/s) for samples with porosity from ~40-60%. The same samples from Jackson and Richardson (2007) had densities from ~1.7-2.0 (g/cm^3) (Table 1).

1.1.11 Seismic Response of Hard Bottom Seafloors

In most instances, the seafloor has high impedance with respect to the water column above it (Sheriff and Geldart, 1995). Typically, the impedance contrast between the water column and seafloor is one of the largest to be detected in marine seismic data, and the reflection coefficient is large (Pritchett, 1990; Sheriff and Geldart, 1995). The term used to describe a large impedance contrast at the water column and seafloor

17

interface is 'hard bottom' seafloor (Pritchett, 1990). According to Yilmaz (2001), a typical reflection coefficient for a strong reflector is ~0.2 and the typical reflection coefficient for a hard bottom seafloor is ~0.3.

If the water column and the seafloor have to high an impedance contrast, most of the seismic energy will be scattered and trapped within the water column (Pritchett, 1990; Matson et al., 1999; Yilmaz, 2001; Jackson and Richardson, 2007). This high impedance contrast bends the angle of the seismic ray paths; the critical angle and refraction angle decrease with increasing seismic impedance contrast (Pritchett, 1990; Yilmaz, 2001). In these cases, where the critical angle and angle of refraction become too low and most of the seismic energy becomes trapped in the water column, very little seismic energy penetrates the rock layers below and imaging of deeper subsurface reflectors is non-existent (Matson et al., 1999; Barkved et al., 2004).

1.2 Data

In November 2014, Texas A&M University acquired marine seismic reflection survey data of offshore Bonaire on the *Le Grand Bleu*. This survey consists of ~172 km of multichannel seismic data recorded on a 150 m-long, 24 channel Geometrics MicroEel streamer. Channel spacing was 6.25 m with 4 hydrophones per channel, leaving a 3.125 m common midpoint (CMP) spacing. The sound source was an Applied Acoustics Dura-Spark 240 sparker system on a CAT300 catamaran. Consisting of 3 arrays of 80 hard-wearing sparker tips, the Dura-Spark 240 sparker system is coupled

with the CSP-N1200 energy source, which delivers a reverse polarity high voltage

charge to the sparker. We towed the sparker and streamer 46 m and 93 m behind the

boat, respectively, with a 47 m near offset. The boat traveled at ~4.0 kn, maintaining a

12.35 m shot interval and a 6 s firing rate. The maximum fold of the survey was 6. The

team acquired a total of 37 individual 2D seismic lines in water depths ranging from

~70-930 m near the coast of Bonaire (Fig. 12). We recorded the raw seismic data using

Geometrics Seismodule Controller (MGOS marine) software and saved the data as SEG-

Y files.

1.3 Methodology

We processed the data using Paradigm Echos 15.1. Data processing steps

included: geometry, spiking deconvolution, spherical divergence correction, filtering,

velocity analysis, stacking, and migration. For detailed processing steps, see Appendix

A. We interpreted the processed seismic lines in two-way-travel time using Paradigm

SeisEarth 15.1 software.

After mapping the seafloor horizon, we grouped the seismic lines by region:

north, central, and south (Fig. 12), and constructed two-way-travel time grids of the

seafloor horizon in the respective regions. We created the two-way-travel time grids in

Paradigm SeisEarth with a Kriging interpolation between the seismic lines.

We calculated the vertical resolution (VR) using the tuning thickness, which

represents the limit of vertical resolution (Sheriff and Geldart, 1995):

$$VR = \frac{\lambda}{4} \quad \text{(Eq.1)}$$

The wavelength (λ) is equal to velocity (v) divided by frequency (f). For this survey, the

dominant frequency is 600 Hz. We used varying velocity values based on varying

lithologic interpretations of the seafloor to calculate the limit of vertical resolution

(Table 2): ~0.67-0.75 m (calcareous sediment), ~1.86-2.71 m (igneous seafloor), and

~1.17-2.92 m (hard limestone seafloor).

2. OBSERVATIONS AND INTERPRETATIONS

2.1 Seismic Response

The acoustic impedance contrast between the water column and seafloor creates the reflection that we interpret as the seafloor, and the amplitude of this reflection records the change in acoustic impedance (Yilmaz, 2001). Equation 2 gives the reflection coefficient, R, which expresses the ratio of amplitudes of this reflection (Yilmaz, 2001):

$$R = \frac{v_2 \rho_2 - v_1 \rho_1}{v_2 \rho_2 + v_1 \rho_1} \text{ (Eq. 2)}$$

The velocity and density of the first layer (the water column in this case) are v_1 and ρ_1 respectively, and the velocity and density of the second layer (the seafloor in this case) are v_2 and ρ_2 respectively.

If the seafloor offshore Bonaire is comprised of igneous rock, and basalt is the predominant lithology, then this would account for a large impedance contrast between the water column and seafloor. Using estimated density and velocity values (Table 1), we calculate the potential reflection coefficient for a seafloor comprised predominantly of a saturated basalt: ~0.83. Similarly, the reflection coefficients is ~0.78 for saturated felsic igneous material, and ~0.81-0.65 for saturated limestone (Table 1). These values are well above the ~0.3 reflection coefficient value for a typical hard bottom seafloor (Yilmaz, 2001). These high magnitude reflection coefficients mean that the seafloor

reflects a majority of energy back into the water column, leaving very little to penetrate the rock layers beneath.

In a majority of the seismic reflection data in this survey, observable reflectors occur at or near the seafloor (Fig. 13). Beneath the seafloor, seismic energy quickly dissipates and subsequent reflectors are non-existent. We interpret the singular appearance of discernible seismic reflectors at or near the seafloor as the likely result of a hard bottom. The singular appearance of discernible seismic reflectors at or near the seafloor in the seismic reflection data supports the interpretation that the possible lithology of the seafloor is likely igneous or limestone. These lithologies would create an impedance contrast at the water column-seafloor interface that is large enough to prevent imaging deeper subsurface reflectors.

The seafloor off Bonaire could be sediment laden. However, we do not interpret a sedimentary seafloor in the majority of our seismic data, as the appearance of a singular seafloor reflector is indicative of a hard bottom substrate. In regards to the layer of sediment referred to as a sand scape (Soest et al., 2014), we interpret that this sediment is not imaged in the majority of our data because it does not produce a reflection. Soest et al. (2014) described a thin, high-porosity sand scape layer at the seafloor in vicinity of the south region. A thin layer of high-porosity, silt-to-sand sized carbonate sediment is common in carbonate hard bottom seafloors, such as off the coast of Florida; this thin layer has little to no impedance contrast with the water column above, and consequently may not produce a reflection (Jackson and Richardson, 2007).

Additionally, the thickness of accumulated seafloor sediment may be below the limit of vertical resolution of the seismic survey.

2.2 Seafloor Topography

Two-way-travel time grids of the seafloor from the seismic data reveal the approximate topography of the seafloor in the study area (Fig. 14). In the north, the contours of the seafloor grid are spaced closer together than the grids in the central or south, indicating that the seafloor is more steeply dipping in the north than in the central and south region (Fig. 14).

In the north, the grid exhibits a shallow topographic high that protrudes out from the northern shore and is flanked on either side by topographic lows (Fig. 14). This topographic pattern superficially resembles an anticline. The onshore topography adjacent to the north grid, which is steep and has an elevation up to 241 m, also resembles an anticline (Fig. 14). Baker (1924) and Hippolyte and Mann (2011) interpreted that the topographic high in the north of Bonaire represented the crest of an anticline trending NW-SE. Our seismic data provides evidence for the continuation of this folded structural deformation offshore where the bathymetric contours superficially resemble an anticline. Based on the contour pattern in the seafloor, we interpret the anticlinal expression to trend NW-SE (Fig. 14). Our offshore interpretation aligns with the interpretation of marine seismic data acquired at a greater distance offshore the north

of Bonaire than our data, where Silver et al. (1975) interpreted the seaflooor topography as a NW-SE trending anticline.

A similar topographic pattern resembling an anticline exists in the southwest portion of the south grid with more shallowly dipping flanks (Fig. 14). Although this southern feature superficially resembles the topographic expression of a WSW-ENE trending anticline, the adjacent onshore topography is broad and nearly flat, and contains no evidence of structural deformation or uplift (Fig. 14). This feature could be an anticline, but due to the lack of deformation in adjacent onshore outcrops, the folding could be representative of an earlier deformational event unrelated and preceding the deformational event expressed in the seafloor topography and adjacent onshore outcrops in the north of Bonaire. Alternatively, this feature could reflect the antecedent topography of the in situ emplacement of the igneous Cretaceous Washikemba Formation of Bonaire.

2.3 Seafloor Discontinuity

The seafloor reflector in the seismic reflection data is laterally continuous except for a limited number of discrete discontinuities. We classify the observable discontinuities in the seafloor by three characteristics:

1. Vertical offset with a discernable break in the seafloor reflector (Figs. 15, 16).

2. Vertical offset with or without a discernable break in the seafloor reflector and sub-vertical reflectors extending into the sub-surface from the seafloor (Figs. 17, 18).

3. Discernable upslope break and offset and overriding seafloor reflectors downslope (Fig. 19).

2.3.1   *Seafloor Vertical Offset with Break in Reflectors*

There are four discontinuities in four seismic profiles that we characterize by vertical offset with a discernable break in the seafloor reflector (Figs. 12, 16). The type example has a break in the seafloor reflector with a vertical offset of ~17 ms and a horizontal offset of ~119 m (Figs. 15, 16a). The seafloor offset has a SE dip direction, however this dip observation, as is the case with all of our dip observations, is constrained by a singular observation from the data in one seismic profile (Fig. 15, 16a). We observe similar features in additional locations (Fig. 16b-d). In Fig. 16b, the data exhibits a vertical seafloor offset of ~89 ms and a horizontal offset of ~146 m, with a NNW dip direction of the offset. Additionaly, the data displays a vertical seafloor offset of ~27 ms and a horizontal offset of ~60 m, with a NW dip direction of the offset (Fig. 16c). We observe a vertical seafloor offset of ~68 ms and a horizontal offset of ~153 m, with a SW dip direction of offset (Fig. 16d). Features in seismic reflection profiles that evidence reflector offset (vertical and horizontal) and distinct breaks in reflector continuity are typically interpreted as faults (Fossen, 2010; Liang et al., 2010).

Therefore, we interpret the distinct breaks and offsets in the seafloor reflectors as faults, with the offsets indicative of normal displacement (Figs. 14, 16).

2.3.2 Seafloor Vertical Offset and Sub-Vertical Reflectors Extending into the Sub-Surface from the Seafloor

There are four discontinuities that we classify as vertical offset with or without a discernable break in the seafloor reflector and sub-vertical reflectors extending into the sub-surface from the seafloor (Figs. 12, 18). The type example does not display a break in the seafloor but the seafloor has a vertical offset of ~28 ms and a horizontal offset of ~31.25 m (Figs. 17, 18a). Sub-vertical reflectors extend into the sub-surface from the seafloor at this location, and both the sub-surface reflectors and seafloor offset have a SW dip direction (Figs. 17, 18a). We observe similar features in additional locations (Fig. 18a-c). In Fig. 18b, the data exhibits a vertical offset of ~48 ms and a horizontal offset of ~172 m. This example displays a clear break between the offset seafloor reflectors and sub-vertical reflectors extending into the sub-surface from the seafloor; both the seafloor offset and sub-surface reflectors have a NE dip direction (Fig. 18b). Additionally, the data displays a vertical offset of ~10 ms and a horizontal offset of ~28 m (Fig. 18c). At this location, the data does not exhibit a distinguishable break in the offset seafloor reflectors but do observe sub-vertical reflectors extend into the sub-surface from the seafloor; both the seafloor offset and sub-surface reflectors have a NW dip direction (Fig. 18c). We observe a vertical offset of ~20 ms and a horizontal offset of

~94 m (Fig. 18d). Sub-vertical reflectors extend into the sub-surface from the offset

seafloor, which displays a discernable break in reflectors; and both the sub-surface

reflectors and seafloor offset have a SW dip direction (Fig. 18d). Features in seismic

reflection profiles that evidence reflector offset (vertical and horizontal) and sub-vertical

reflectors extending into the sub-surface from the seafloor, are typically interpreted as

faults (Sheriff and Geldart, 1995; Mondziel, 2007). Therefore, we interpret these offsets

and discontinuities in the seafloor reflectors as faults, with the offsets indicative of

normal displacement (Figs. 14, 16a-d). Additionally, because the sub-vertical reflectors

occur at discontinuities and offsets we interpret as faults, we interpret the sub-seafloor

reflectors to be part the fault plane. We suggest that we image these fault planes and not

others in the data set, due to a combination of sediment and water filling the planes,

which provides a reflection-producing surface where one otherwise would not exist.

2.3.3 Upslope Break and Offset and Downslope Package

There is one seafloor discontinuity with a significant discernable seafloor break

and downslope package (Fig. 19). The seafloor reflector breaks with an ~65 ms vertical

offset and an ~81 m horizontal offset. Beneath the offset seafloor, the data displays a

concave up sub-surface reflector that appears sub-vertical close to the seafloor, but

changes inclination and appears sub-horizontal as vertical and horizontal offset increase

(Fig. 19). Both the sub-surface reflectors and seafloor offset have a NW dip direction

(Fig. 19). Downslope of the seafloor offset, the data shows a package with the sub-

27

seafloor reflector as the base, and the seafloor reflector as the top. Beneath the package, the basal reflector is of relatively high amplitude (Fig. 19). The lateral extent of the package is ~56 m. At the downslope extent of the package, we observe an additional seafloor offset, with the toe of the package rising up over the downslope seafloor ~61 ms. These features are typical characteristics of a submarine rotational slump, which are ubiquitous on coastal slopes globally (Smith et al., 1999; Martinez et al., 2005). We suggest that the downslope package is the slump deposit, the upslope seafloor offset is the scarp, and the downslope offset represents the toe of the rotational slump deposit popping up over the downslope seafloor (Fig. 19).

2.3.4 NW-SE Striking Faults

There are four instances of NW-SE-striking faults offshore Bonaire (Figs. 16d, 18a-b,d). The NW-SE-striking fault in Fig. 18a occurs in close proximity, <1 km, to the NW-SE-striking fault in Fig. 18d (Figs. 12, 20). The faults have the same SW direction of offset, and both faults display sub-vertical reflectors extending into the sub-surface from the seafloor (Fig 18a, d). Because of the proximity and similarities of the NW-SE-striking faults in Fig. 18a and 18d we interpret the faults to be part of the same fault plane (Fig. 20). Although we are able to correlate these faults (Fig 18a, d), we are unable to correlate other NW-SE-striking faults based on proximity or visual appearance.

In the adjacent basins offshore the ABCs, Gorney et al. (2007) observed recent seafloor offsets along the NW-SE striking Oligocene-Holocene faults. Hippolyte and

Mann (2011) interpreted the recent seafloor offsets identified by Gorney et al. (2007) to indicate a present NE-SW extensional tectonic regime. To see if the NW-SE-striking faults in our data relate to a present NE-SW extensional tectonic regime and the NW-SE-striking faults identified by Gorney et al. (2007), we calculate an estimated dip angle of the faults planes in our data and compare it to the angles presented by Gorney et al. (2007).

We estimate the dip of the faults using the sub-vertical reflectors extending into the sub-surface that we identify as the fault planes, because these provide greater certainty to the direction and extent of the NW-SE striking faults. Therefore, we only estimate the angle of the fault planes in Fig. 18a, 18b, and 18d, but not Fig. 16d. Since we interpret the NW-SE-striking faults in seismic Fig. 18a and 18d to be part of the same fault plane, we calculate the angle for this fault plane using just the sub-vertical reflectors from the fault in Fig. 18a because we image the fault better in Fig. 18a then in Fig. 18d.

Because of the quality of the data, the sub-vertical reflectors appear as wide reflectors with an unclear termination point, and the exact location and direction of the fault plane is not known. To account for this unknown, we propose three varying fault plane locations within the sub-vertical reflectors to cover the possible direction and location the fault plane could occur (Fig. 21). The proposed fault planes all start at the same water bottom location (two-way-travel time and CMP number) on the hanging wall, however the termination point of the fault plane varies in that we maintain a

constant ending two-way-travel time but change the CMP number (Fig. 21) (Tables 3, 4).

To calculate the dip of the proposed fault planes, we first need to convert our two-way-travel time (TWT) start and endpoints into depth (meters) below sea level using assumed velocity values. Because the first point of the proposed fault planes occur at the water bottom, we multiply the velocity of water, 1500 m/s, by the water bottom TWT, measured in seconds, to find the depth of the seafloor below sea level (Tables 3, 4). The termination point of the fault plane occurs within the lithology of the seafloor and subsurface, and therefore to calculate the depth of the fault plane termination points, we multiply the end member velocity values (m/s) of the hard limestone and igneous lithologies that could possibly exist at or below seafloor off the coast of Bonaire by the TWT (s) values of the fault plane termination points (Table 3, 4). We convert the CMP numbers into a location, a length in meters from the start of the line, by multiplying the CMP number by the CMP offset of 3.125 m.

With the TWT values converted to a meters depth below sea level and the CMP numbers converted to a location in meters along the line, we use geometry and algebra to fine the slope and angle of the fault plane (Fig. 22). We find the slope, m, of the fault plane using the equation:

$$m = \frac{y_2 - y_1}{x_2 - x_1} \text{ (Eq. 3)}$$

The depth below sea level of the termination point of the fault plane is x_1, the CMP location of the termination point of the fault plane is y_1, the depth below sea level of the start point of the fault plane at the seafloor is x_2, and the CMP location of the start point

30

of the fault plane at the seafloor is y_2 (Fig. 22) (Tables 3, 4). We find the angle, θ, from

horizontal, the seafloor, of the fault using the equation:

$$\theta = arctan(m) \quad \text{(Eq. 4)}$$

The slope of the fault plane is m. (Fig. 22) (Tables 3, 4). For the NW-SE-striking fault in

Fig. 18b, we calculate that this fault could dip anywhere from ~80-53° depending on

where we interpret the fault plane to occur and the different lithology values (Table 3).

For the NW-SE-striking fault plane in Fig. 18a, we calculate that this fault could dip

anywhere from ~86-69° depending on where we interpret the fault plane to occur and the

different lithology values (Table 4).

3. DISCUSSION

3.1 Past Deformation on Bonaire

3.1.1 Topographic Expression of an Anticline Nearshore Northern Bonaire

Based on new data, we interpret a NW-SE trending anticline in the seafloor directly adjacent to the north of the island, which aligns with the data from several previous studies (Fig. 14) (Baker, 1924; Silver et al., 1975; Hippolyte and Mann, 2011). Baker (1924) and Hippolyte and Mann (2011) interpreted an anticline on Bonaire based on onshore geologic data, while Silver et al. (1975) interpreted an anticline offshore northern Bonaire based on three seismic lines acquired ~8-17 km offshore in deep water. Our data, which spans from ~250 m to ~3.5 km off the coast of Bonaire, provides nearshore evidence for an anticline that links the onshore interpretations of Baker (1924) and Hippolyte and Mann (2011) to the offshore interpretation of Silver et al. (1975). We suggest that the anticline onshore the island of Bonaire reflects a much larger anticline structure that extends offshore up to at least ~17 km based on our data and the interpretation from Silver et al. (1975).

The aforementioned workers regionally interpreted large NW-SE trending anticlines on and offshore Aruba and Curaçao as well. Because the ABCs are relatively close in geographic proximity and share almost all of the same geologic formations, Hippolyte and Mann (2011) proposed that the similar trends of the NW-SE trending

anticlines on each of the islands must be the result of the same regional folding event. Hippolyte and Mann (2011) also suggested that the similar inclinations of the Miocene-Pliocene Seroe Domi Formation on all of the ABCs, which dips steeply at 28-38°, must have a singular cause. Based on onshore outcrops, Hippolyte and Mann (2011) concluded that the inclination of the Seroe Domi Formation was the result of post-depositional deformation and proposed the inclination occurred contemporaneously with the regional folding event responsible for the NW-SE trending anticlines. With this correlation, Hippolyte and Mann (2011) dated the anticlines on the ABCs to after the deposition of the Seroe Domi Formation and constrained the anticlines to be the product of NNE-SSW-directed Pliocene-Quaternary compression. Because we correlate the offshore anticline in our data to the onshore anticline on Bonaire, we conclude that the anticline in our data is representative of the regional NNE-SSW-directed Pliocene-Quaternary compression responsible for the NW-SE trending anticline on Bonaire as well as the NW-SE trending anticlines Aruba and Curaçao.

The seafloor data off the north of Bonaire from this study not only aligns with the regional Pliocene-Quaternary compression, but also fills the data gap between and confirms the similar NW-SE trending anticline interpretations on and offshore Bonaire by previous authors.

3.1.2 Topographic Expression of an Anticline in the South Seafloor

In addition to the anticline in the north region, we also identify a possible anticline in the south region seafloor trending WSW-ENE (Fig. 14). Unlike the north region, the onshore topography adjacent to the south region, which is broad and nearly flat with a maximum elevation of ~6 m, does not indicate an anticline as there is no evidence of structural uplift or deformation (Fig. 14). It possible that this feature does not reflect direct structural deformation, but is rather related to antecedent topography from the in situ emplacement of the igneous Cretaceous basement of Bonaire, the Washikemba Formation. Alternatively, while the present onshore topography in the south does not resemble or support the presence of a WSW-ENE trending anticline in the adjacent seafloor, it is possible that this feature could be related to earlier folding.

The current trend of the possible anticline in the seafloor in the south is WSW-ENE, which means a NW-SE to NNW-SSE-directed compression would be responsible for its formation. Beardsley and Avé Lallemant (2007) proposed a NW-SE-directed late Paleogene compression regionally affecting the Cretaceous basement, the Washikemba Formation, of the ABCs. Hippolyte and Mann (2011) also suggested the same regional NW-SE-directed late Paleogene compression. If this is an anticline in the seafloor in the south, then its formation could correspond to the NW-SE-directed late Paleogene compression that effected the Washikemba Formation. Additionally, Beardsley and Avé Lallemant (2007) predict 15° of clockwise rotation of the ABCs since the late Oligocene-early Miocene, which means that the possible anticline in the south would

have initially trended to the SW-NE. This possible initial SW-NE trend of the anticline

corresponds to the regional NW-SE-directed late Paleogene compression.

There are two possible interpretations for the topographical expression of an

anticline in the south seafloor; it is the result of the antecedent topography of the igneous

basement of Bonaire or it is the result of NW-SE-directed late Paleogene compression.

With our data alone, we do not have the evidence to substantiate one

interpretation over the other, however we believe that future work (e.g drilling cores

perpendicular to the axis of this feature) could shed light on the origin of the feature.

3.2 Present Day Deformation on Bonaire

3.2.1 Slide-Induced Faulting

We observe a discontinuity that is the result of an underwater landslide (Fig 19).

We propose a possible relationship between the slide in Fig. 19 and the two surface

faults at the seafloor that occur upslope of this slide (Figs. 16c, 18c, 23). Because these

faults (Fig. 14) occur directly upslope, we suggest that these faults are the result of the

same process that influenced the landslide. While the seafloor has not significantly failed

at these features compared to the down slope slide, we interpret that the features in Figs.

16c, 18c could be an incipient seafloor failure.

Additionally, we propose a possible relationship between the slide scarp in Fig.

19 and the fault in Fig. 16a (Fig. 20). Both features display significant seafloor offset,

~89 ms in Fig. 19 and ~65 ms in Fig. 16a; and have an approximate NW-NNW offset direction. Additionally, both features strike approximately NE-SW, and are located ~1 km apart (Fig. 20). We argue that the close proximity of the features and similar characteristics to be an indication that the features are part of the same slide plane (Fig. 20). Since Fig. 19 is a slide scarp that results from block sliding, we hypothesize Fig. 16b to be a scarp from the same slide feature. This hypothesis of Fig. 16b is an alternative to the previous fault interpretation. We suggest that we do not image the slide deposit in Fig. 16b, while we do in Fig. 19, due to the location and orientation of the seismic profiles on the slope with respect to the slide deposit (Fig. 12).

Bales (2016) showed multiple submarine slides on Bonaire, some of which are similar in character and thereby support seafloor landslides on Bonaire.

The processes involved in inducing submarine landslides vary among individual landslides, and processes rarely fit pre-established categories (Canals et al., 2004). Canals et al. (2004) noted that the final trigger mechanisms for submarine landslides is often assumed to be earthquakes, but noted that other destabilization process could trigger submarine landslides as well. While we do not rule out the possibility of an earthquake triggered landslide for the submarine slope of Bonaire, as the region presently experiences intermittent earthquake seismicity and paleo-tsunami deposits on Bonaire indicate nearby earthquakes throughout the Holocene (Engel et al., 2010), we suggest two alternative mechanisms for submarine landslides.

On the Adriatic Coast of central Italy, Della Seta et al. (2013) interpreted the Vasto Landslide to be caused by the progressive tectonic uplift of the coast. Herweijer

and Focke (1978) proposed that Bonaire has been experiencing a small magnitude of uplift since the Pleistocene. If uplift of the Bonaire is occurring, then this could be a possible trigger for submarine sliding.

In Nevada, Hurst et al. (1985) observed block sliding and surface faults along the ramp of a Silurian carbonate platform which they believed to be the result of subsidence. On Bonaire, Sulaica (2015) observed that the first Pleistocene carbonate terrace is located above sea level in the north of the island but located below sea level in the south of the island, and argued this to be the result of recent subsidence in the south. If subsidence is occurring in the south, then this could be alternative possible explanation for the sliding and surface faulting (Fig. 23).

3.2.2 NW-SE Striking Faults

Gorney et al. (2007) observed that the NW-SE-striking Oligocene-Holocene normal faults of had dips that ranged from 50-60°. The dips we estimate for the NW-SE-striking faults in our data are predominately of a higher magnitude, however a few of our angle estimations are near the range of angles observed by Gorney et al. (2007). For the fault plane in Fig. 18a, the shallowest angle we estimate is ~69° using the low-end velocity value of a hard limestone lithology (Table 4). In Fig. 18b, we estimate the shallowest angles of the fault plane between 69-53° using the low-end velocity value of a hard limestone lithology (Table 3). If the lithology at or below the seafloor is a hard limestone with a low velocity value, then it is possible that these low-end angle

37

estimations in Fig. 18a and 18b are related to the angles of the NW-SE faults interpreted by Gorney et al. (2007). Additionally, if the NW-SE-striking faults in our data do relate to the NW-SE-striking faults identified by Gorney et al. (2007), then our faults would indicate a present NE-SW extensional tectonic regime in agreeance with present tectonic regime proposed by Hippolyte and Mann (2011).

If the majority of dip angles we estimate for the NW-SE faults are steeper than the NW-SE faults identified by Gorney et al. (2007), could the faults from this study still relate to the same recent NE-SW extension affecting the NW-SE faults identified by Gorney et al. (2007)?

The NW-SE faults in our data could be a local response to the present regional extension and not part of the same regional NW-SE fault planes identified Gorney et al. (2007), which means they could have a different angle. We propose that the NW-SE faults in our data would not move at the same angle as the faults by Gorney et al. (2007) because the faults identified by Gorney et al. (2007) originated during the late Oligocene-early Miocene and were reactivated recently. Therefore the recent movement on the NW-SE faults identified by Gorney et al. (2007) would occur on the fault plane that maintains the angle from the previous late Oligocene-early Miocene faulting. Additionally, Beardsley and Avé Lallemant (2007) predict 15° of clockwise rotation of the ABCs since the late Paleogene which could also affect the angle of the faults identified by Gorney et al. (2007). Various models propose that normal faults can initiate at steeper angles and rotate to shallower angles (Olive and Behn, 2014). It is possible that the NW-SE faults identified by Gorney et al. (2007) initiated at a steeper angle more

in line with our higher angle estimations (Tables 3, 4), and rotated to a present shallower angle.

A second question that arises from relating the NW-SE faults from our data to present regional deformation is why can the NW-SE faults in our data not be traced longer than 1 km? If NW-SE faults in our data are the result of regional deformation, we would expect these fault trends to be traceable over long distances. In the nearby fold-thrust belt of the inverted Falcón sedimentary basin, N-NE trending folds can be traced over ~200 km (Fig. 5). Similarly, the faults in the offshore sedimentary basin of the Le Vela fold-thrust belt can be traced over a distance of ~175 km, and the NW-SE faults of fault family 2 interpreted by Gorney et al. (2007) can be traced over ~100 km in the adjacent sedimentary basins to the ABCs (Fig. 5). In the regional sedimentary basins near the ABCs we observe faults traced over many tens kilometers, but nearshore Bonaire and onshore the ABCs we cannot observe faults longer than a few km; because of this, we suggest that regional deformation does not affect the hard rock lithology of Bonaire and the islands of the ABCs in the same manner it affects the adjacent sedimentary basins.

3.2.3 Comparison with Previous Structure Analysis

Some magnitude of recent regional deformation affects the ABCs based on the uplift of the Pleistocene carbonate terraces on all of the islands (Herweijer and Focke, 1978; Sulaica, 2015). However, the present day regional stress across the Bonaire Block

and the ABCs is not well constrained. Some past workers have argued the regional stress affecting the ABCs is compression (De Buisonjé, 1974; Schubert and Scheidegger, 1986), while other past workers have proposed extension as the regional stress affecting the ABCs (Audemard et al., 2005; Hippolyte and Mann, 2011).

Some of the faults in our data appear related to the regional tectonics. In the previous section, *3.2.2*, we tie the NW-SE trending faults in our data to regional tectonics based on similar strikes and similar possible angle estimations of these faults. Conversely, we interpret the faults that do not strike NW-SE in our data to be related to local deformation.

The fault in Fig. 16a is the only fault we interpret in the central region (Figs. 12, 14). While the fault in Fig. 16a strikes NE-SW like the faults in Figs. 16c and 18c, the offset of the fault Fig. 16a is to the SE whereas the offset of the faults in Figs. 16c and 18c are to the NW. Based on the proximity and characteristics of the fault in Fig. 16a, we believe this fault is a restricted fault and do not link it with any of the other faults in our data. However, we do correlate the fault in Fig. 16a with the other faults in the data that do not strike NW-SE (Figs. 16c,18c), in that we hypothesize that the fault in Fig. 16b could be the result of local deformation like we argue for the two other faults that do not strike NW-SE.(Figs. 16c,18c). The faults in our data that do not strike NW-SE cannot be explained by regional deformation and correlate to localized deformational processes on Bonaire (e.g. rotational slumps or slope failure). This interpretation lends confidence to our interpretation that the NW-SE trending faults are related to regional faults and not local deformation.

40

If some of the faults in our data are in fact related to regional tectonics, e.g. the NW-SE trending faults (Figs. 16d, 18a, c-d), then our fault analysis would be consistent with the interpretations of previous authors that the present regional stress regime is extension. The NW-SE trending faults in our data conform to present regional extension as the faults are normal faults.

4. CONCLUSIONS

We conclude that the interpreted anticline of this study in the north is the same anticline described by previous authors in adjacent locations, and that this anticline extends from onshore the north of Bonaire to at least ~17 km offshore.

We conclude that there are two likely interpretations for the topographical expression of an anticline in the south seafloor:

1. The topographic expression reflects the in situ emplacement of the igneous Cretaceous basement of Bonaire, the Washikemba Formation.

2. The topographic expression reflects NW-SE-directed late Paleogene compression that resulted in SW-NE trending anticline that was rotated clockwise 15° into its present WSW-ENE trend.

We interpret a submarine rotational slump offshore Bonaire, and while we do not rule out the possibility of an earthquake as the mechanism for causing the rotational slump, we suggest two potential alternative mechanisms for the rotational slump: uplift of the entire island of Bonaire or subsidence of the south of Bonaire.

We conclude that the NW-SE-striking faults could be related to the NW-SE-striking faults identified by Gorney et al. (2007), and are likely the result of a present regional NE-SW-directed compression

We suggest that the faults in our data that do not strike NW-SE cannot be explained by regional deformation and correlate to localized deformational processes on Bonaire (e.g. rotational slumps or slope failure). Additionally, we conclude that NW-SE

trending faults support a present regional extension, which in turn supports the

hypothesis of Hippolyte and Mann (2011) that footwall uplift of reactivated normal

faults is the mechanism for recent uplift of the ABCs.

5. SUMMARY AND IMPLICATIONS

The island of Bonaire has a complex tectonic history; this study uses an integration of 2D marine seismic reflection data acquired nearshore, off the west coast of Bonaire, and previous structural studies to interpret deformation on the island. The study details what processes are likely imparting stress in this environment and contributing to deformation. We seismically observe a large anticline onshore and offshore the north of Bonaire that appears to be the result of regional deformation. Additionally, we identify a rotational slump of the hard rock seafloor due to either localized uplift of the island or subsidence of the south portion of the island. Finally, the faults in the nearshore geology of Bonaire appear to be the result of both regional and local stress. The NW-SE trending faults appear to be the result of a present regional NE-SW extension which provides insight into the poorly constrained present day regional stress. All of the faults not striking NW-SE appear to be the product of local processes like slope failure. These findings highlight three broad implications.

First, although there are many theories regarding the complex tectonics of the Caribbean-South American plate interaction, the present regional tectonics affecting the ABCs is unknown. This study shows the utility of a localized inexpensive high-resolution seismic study to fill in knowledge gaps and further constrain the tectonics of the Caribbean-South American plate interaction. The deformation on Bonaire helps to elucidate the larger regional tectonic story, as well as show how the regional tectonics story affects the local environment, like Bonaire.

44

Second, factors influencing material failure on unsedimented hard rock marine slopes are poorly constrained. These slope failures on Bonaire are relatively easy to access and study due to the water depth and proximity to the coastline. This study shows what factors potentially influence these failures, which is important for understanding the process of hard rock slope failure in more difficult to reach environments. Illuminating the underlying contributions to this process is critically important, especially in areas with large population, such as Hawaii and Maldives, where these events can cause loss of life and property.

Finally, understanding what deformation is present on Bonaire and what stresses are imparting the observed strain, can serve as an aid to the inhabitants of the island to mitigate risk. The faulting offshore Bonaire is not widespread but still prevalent and indicates Bonaire is susceptible to the effects of present regional tectonics.

REFERENCES

Alexander, C. S., 1961, The Marine Terraces of Aruba, Bonaire, and Curacao,

    Netherlands Antilles: Annals of the Association of American Geographers, v. 51,

    no. 1, p. 102-123.

Audemard, F. A., 2001, Quaternary tectonics and present stress tensor of the inverted

    northern Falcon Basin, northwestern Venezuela: Journal of Structural Geology,

    v. 23, no. 2-3, p. 431-453.

Audemard, F. A., Romero, G., Rendon, H., and Cano, V., 2005, Quaternary fault

    kinematics and stress tensors along the southern Caribbean from fault-slip data

    and focal mechanism solutions: Earth Science Reviews, v. 69, p. 181-233.

Bak, R. P. M., 1977, Coral reefs and their zonation in Netherlands Antilles: Studies in

    Geology [Tulsa], no. 4, p. 3-16.

Baker, H. B., 1924, Land and freshwater molluscs of the Dutch Leeward Islands:

    Occasional Papers of the Museum of Zoology, University of Michigan, no. 152,

    p. 1-160.

Bales, M., 2016, Geophysical Analysis of Quaternary Marine Sedimentary Processes,

    Bonaire, Netherland Antilles [Masters: Texas A&M University

Bandoian, C. A., and Murray, R. C., 1974, Pliocene-Pleistocene Carbonate Rocks of

    Bonaire, Netherlands Antilles: Geological Society of America Bulletin, v. 85, no.

    8, p. 1243-1252.

Barkved, O., Bartman, B., Compani, B., Gaiser, J., Van Dok, R., Johns, T., Kristiansen, P., Probert, T., and Thompson, M., 2004, The many facets of multicomponent seismic data: Oilfield Review, v. 16, no. 2, p. 42-56.

Barrett, P. J., and Froggatt, P. C., 1978, Densities, porosities, and seismic velocities of some rocks from Victoria Land, Antarctica: New Zealand Journal of Geology and Geophysics, v. 21, no. 2, p. 175-187.

Beardsley, A. G., and Avé Lallemant, H. G., 2007, Oblique collision and accretion of the Netherlands Leeward Antilles to South America: Tectonics, v. 26, no. 2, p. 1-26.

Beets, D. J., MacGillavry, H. J., and Klaver, G., 1977, Geology of the Cretaceous and Early Tertiary of Bonaire: Guide to the field excursions on Curaçao, Bonaire and Aruba, Netherlands Antilles: 8th Caribbean Geological Conference, v. 1, no. 2, p. 18-28.

Beets, D. J., Maresch, W. V., Riaver, G. T., Mottana, A., Bocchio, R., Beunk, F. F., and Monen, H. P., 1984, Magmatic rock series and high-pressure metamorphism as constraints on the tectonic history of the southern Caribbean: Geological Society of America Memoirs, v. 162, p. 95-130.

Bezada, M. J., Schmitz, M., Jacome, M. I., Rodriguez, J., Audemard, F., and Izarra, C., 2008, Crustal structure in the Falcon Basin area, northwestern Venezuela, from seismic and gravimetric evidence: Journal of Geodynamics, v. 45, no. 4-5, p. 191-200.

Biju-Duval, B., Mascle, A., Rosales, H., and Young, G., 1982, Episutural Oligo-
Miocene basins along the North Venezuelan margin: AAPG Memoir, v. 34, p.
347-358.

Boschman, L. M., van Hinsbergen, D. J. J., Torsvik, T. H., Spakman, W., and Pindell, J.
L., 2014, Kinematic reconstruction of the Caribbean region since the Early
Jurassic: Earth-Science Reviews, v. 138, p. 102-136.

Bruggemann, J. H., 1995, Parrotfish grazing on coral reefs : a trophic novelty [PhD:
Rijksuniversiteit Gronigen, 215 p.

Burke, K., 1988, Tectonic evolution of the Caribbean: Annual Review of Earth and
Planetary Sciences, v. 16, p. 201-230.

Canals, M., Lastras, G., Urgeles, R., Casamor, J. L., Mienert, J., Cattaneo, A., De Batist,
M., Haflidason, H., Imbo, Y., Laberg, J. S., Locat, J., Long, D., Longva, O.,
Masson, D. G., Sultan, N., Trincardi, F., and Bryn, P., 2004, Slope failure
dynamics and impacts from seafloor and shallow sub-seafloor geophysical data:
case studies from the COSTA project: Marine Geology, v. 213, no. 1–4, p. 9-72.

Colmenares, L., and Zoback, M. D., 2003, Stress field and seismotectonics of northern
South America: Geology [Boulder], v. 31, no. 8, p. 721-724.

De Buisonjé, P. H., 1974, Neogene and Quaternary Geology of Aruba, Curaçao, and
Bonaire, Utrecht, Utrecht : Natuurwetenshappelijke Studiekring, Publications of
the Foundation for Scientific Research in Surinam and the Netherlands Antilles,
No. 78, 291 p.:

Deffeyes, K. S., Lucia, F. J., and Weyl, P. K., 1965, Dolomitization of Recent and Plio-Pleistocene sediments by marine evaporite waters on Bonaire, Netherlands Antilles: Special Publication - Society of Economic Paleontologists and Mineralogists, p. 71-88.

Della Seta, M., Martino, S., and Scarascia Mugnozza, G., 2013, Quaternary sea-level change and slope instability in coastal areas: Insights from the Vasto Landslide (Adriatic coast, central Italy): Geomorphology, v. 201, p. 462-478.

DeMets, C., Jansuma, P. E., Mattioli, G. S., Dixon, T. H., Farina, F., Bilham, R., Calais, E., and Mann, P., 2000, GPS geodetic constraints on Caribbean-North America Plate motion: Geophysical Research Letters, v. 27, no. 3, p. 437-440.

Engel, M., Brückner, H., Wennrich, V., Scheffers, A., Kelletat, D., Vött, A., Schäbitz, F., Daut, G., Willershäuser, T., and May, S. M., 2010, Coastal stratigraphies of eastern Bonaire (Netherlands Antilles): New insights into the palaeo-tsunami history of the southern Caribbean: Sedimentary Geology, v. 231, no. 1-2, p. 14-30.

Escalona, A., and Mann, P., 2011, Tectonics, basin subsidence mechanisms, and paleogeography of the Caribbean-South American plate boundary zone: Marine and Petroleum Geology, v. 28, no. 1, p. 8-39.

Escalona, A., and Yang, W., 2013, Impact of low-angle subduction in petroleum systems along the Leeward Antilles island arc emergent gas trend, northern South America: First Break, v. 31, no. 5, p. 55-63.

Fossen, H., 2010, Structural geology, United Kingdom, Cambridge University Press : Cambridge, United Kingdom.

Gorney, D., Escalona, A., Mann, P., Magnani, M. B., and Group, B. S., 2007, Chronology of Cenozoic tectonic events in western Venezuela and the Leeward Antilles based on integration of offshore seismic reflection data and on-land geology: AAPG Bulletin, v. 91, no. 5, p. 653-684.

Hall, D. B., 1999, The geomorphic evolution of slopes and sediment chutes on forereefs: Geomorphology, v. 27, no. 3-4, p. 257-278.

Hamilton, E. L., 1978, Sound velocity–density relations in sea-floor sediments and rocks: The Journal of the Acoustical Society of America, v. 63, no. 2, p. 366-377.

Herweijer, J. P., De Buisonjé, P. H., and Zonneveld, J. I. S., 1977, Neogene and Quaternary geology and geomorphology, Guide to the field excursions on Curaçao, Bonaire and Aruba, Netherlands Antilles, Volume 1: Amsterdam, Stichting GUA, Geologisch Institut, p. 49-55.

Herweijer, J. P., and Focke, J. W., 1978, Late Pleistocene depositional and denudational history of Aruba, Bonaire and Curacao (Netherlands Antilles): Geologie en Mijnbouw. Netherlands Journal of Geosciences, v. 57, no. 2, p. 177-187.

Hippolyte, J.-C., and Mann, P., 2011, Neogene–Quaternary tectonic evolution of the Leeward Antilles islands (Aruba, Bonaire, Curaçao) from fault kinematic analysis: Marine and Petroleum Geology, v. 28, no. 1, p. 259-277.

Hurst, J. M., Sheehan, P. M., and Pandolfi, J. M., 1985, Silurian carbonate shelf and
slope evolution in Nevada: A history of faulting, drowning, and progradation:
Geology, v. 13, no. 3, p. 185-188.

Hyndman, R. D., and Drury, M. J., 1976, The physical properties of oceanic basement
rocks from deep drilling on the Mid-Atlantic Ridge: Journal of Geophysical
Research, v. 81, no. 23, p. 4042-4052.

Jackson, D. R., and Richardson, M. D., 2007, High-frequency seafloor acoustics
Underwater acoustics, United States, Springer : New York, NY, United States.

Jackson, T. A., and Robinson, E., 1994, The Netherlands and Venezuelan Antilles:
Jamaica, University of the West Indies Publisher's Association : Kingston,
Jamaica, p. 249-263.

Kaniuth, K., Drewes, H., Stuber, K., Tremel, H., Hernández, N., Hoyer, M.,
Wildermann, E., Kahle, H.-G., Geiger, A., and Straub, C., 1998, Crustal
Deformation along the Caribbean — South American Plate Boundary Derived
From The Casa GPS Project, *in* Forsberg, R., Feissel, M., and Dietrich, R., eds.,
Geodesy on the Move: Gravity, Geoid, Geodynamics and Antarctica: Berlin,
Heidelberg, Springer Berlin Heidelberg, p. 417-422.

Keller, B., 2011, Imaging the twilight zone: the morphology and distribution of
mesophotic zone features, a case study from Bonaire, Dutch Caribbean [M.S.:
University of Delaware, 181 p.

Kellogg, J. N., 1984, Cenozoic tectonic history of the Sierra de Perija, Venezuela-
Colombia, and adjacent basins: Memoir - Geological Society of America, v. 162,
p. 239-261.

Keppie, D. F., 2014, The Analysis of Diffuse Triple Junction Zones in Plate Tectonics
and the Pirate Model of Western Caribbean Tectonics, Springer New York,
SpringerBriefs in Earth Sciences, 75 p.:

Klaver, G., 1976, The Washikemba Formation, Bonaire [M.S.: University of Utrecht,
128 p.

Kroehler, M. E., Mann, P., Escalona, A., and Christeson, G. L., 2011, Late Cretaceous-
Miocene diachronous onset of back thrusting along the South Caribbean
deformed belt and its importance for understanding processes of arc collision and
crustal growth: Tectonics, v. 30, no. 6, p. 31.

Liang, L., Hale, D., and Maucec, M., 2010, Estimating Fault Displacements In Seismic
Images, 2010 SEG Annual Meeting: Denver Colorado, Society of Exploration
Geophysicists.

Martinez, J. F., Cartwright, J., and Hall, B., 2005, 3D seismic interpretation of slump
complexes: examples from the continental margin of Israel: Basin Research, v.
17, no. 1, p. 83-108.

Matson, K. H., Paschal, D., and Weglein, A. B., 1999, A comparison of three multiple-
attenuation methods applied to a hard water-bottom data set: Leading Edge
[Tulsa, OK], v. 18, no. 1, p. 120.

Mondziel, S., 2007, Morphology, Structure, and Tectonic Evolution of the Mona

    Canyon, Puerto Rico [Masters of Science: University of North Carolina

    Wilmington, 93 p.

Muhs, D. R., Pandolfi, J. M., Simmons, K. R., and Schumann, R. R., 2012, Sea-level

    history of past interglacial periods from uranium-series dating of corals, Curaçao,

    Leeward Antilles islands: Quaternary Research, v. 78, no. 2, p. 157-169.

Neill, I., Kerr, A. C., Hastie, A. R., Stanek, K.-P., and Millar, I. L., 2011, Origin of the

    Aves Ridge and Dutch–Venezuelan Antilles: interaction of the Cretaceous 'Great

    Arc' and Caribbean–Colombian Oceanic Plateau?: Journal of the Geological

    Society, v. 168, no. 2, p. 333-348.

Olive, J.-A., and Behn, M. D., 2014, Rapid rotation of normal faults due to flexural

    stresses: An explanation for the global distribution of normal fault dips: Journal

    of Geophysical Research: Solid Earth, v. 119, no. 4, p. 3722-3739.

Pérez, O. J., Bilham, R., Bendick, R., Velandia, J. R., Hernández, N., Moncayo, C.,

    Hoyer, M., and Kozuch, M., 2001, Velocity field across the Southern Caribbean

    Plate Boundary and estimates of Caribbean/South-American Plate Motion using

    GPS Geodesy 1994–2000: Geophysical Research Letters, v. 28, no. 15, p. 2987-

    2990.

Perry, C. T., Edinger, E. N., Kench, P. S., Murphy, G. N., Smithers, S. G., Steneck, R.

    S., and Mumby, P. J., 2012, Estimating rates of biologically driven coral reef

    framework production and erosion; a new census-based carbonate budget

methodology and applications to the reefs of Bonaire: Coral Reefs, v. 31, no. 3, p. 853-868.

Pijpers, P. J., 1933, Geology and paleontology of Bonaire (D. W. I.), Utrecht, Utrecht: Oosthoek, Geographic and Geological Announcements. Physiograpical-Geological Series, No. 8, 103 p.:

Pindell, J., Maresch, W. V., Martens, U., and Stanek, K., 2012, The Greater Antillean Arc: Early Cretaceous origin and proposed relationship to Central American subduction mélanges: implications for models of Caribbean evolution: International Geology Review, v. 54, no. 2, p. 131-143.

Porras, L., Evolución tectónica y estilos estructurales de la región Costa Afuera de las Cuencas de Falcón y Bonaire, *in* Proceedings VII Simposio Bolivariano. Exploración Petrolera de las Cuencas Subandinas, Memoria, Caracas, Venezuela, 2000, p. 279-292.

Priem, H. N. A., Beets, D. J., and Verdurmen, E. A. T., 1986, Precambrian rocks in an early Tertiary conglomerate on Bonaire, Netherlands Antilles (southern Caribbean borderland); evidence for a 300 km eastward displacement relative to the South American mainland ?: Geologie en Mijnbouw. Netherlands Journal of Geosciences, v. 65, no. 1, p. 35-40.

Pritchett, W. C., 1990, Acquiring better seismic data, United Kingdom, Chapman and Hall : London, United Kingdom.

Salisbury, M., and Christensen, N. I., 1978, The seismic velocity structure of a traverse through the Bay of Islands ophiolite complex, Newfoundland, an exposure of

oceanic crust and upper mantle: Journal of Geophysical Research, v. 83, no. B2, p. 805-817.

Schellmann, G., Radtke, U., Scheffers, A., Whelan, F., and Kelletat, D., 2004, ESR Dating of Coral Reef Terraces on Curaçao (Netherlands Antilles) with Estimates of Younger Pleistocene Sea Level Elevations: Journal of Coastal Research, p. 947-957.

Schubert, C., and Scheidegger, A. E., 1986, Recent Joints and Their Tectonic Significance in the Coastal Range of Venezuela and in Curacao: Journal of Coastal Research, v. 2, no. 2, p. 167-172.

Schubert, C., and Szabo, B. J., 1978, Uranium-series ages of pleistocene marine deposits on the islands of Curacoa and La

Blanquilla, Caribbean Sea: Geologie en Mijnbouw. Netherlands Journal of Geosciences, v. 57, no. 2, p. 325-332.

Sheriff, R. E., and Geldart, L. P., 1995, Exploration seismology, United Kingdom, Cambridge University Press, United Kingdom.

Silver, E. A., Case, J. E., and MacGillavry, H. J., 1975, Geophysical study of the Venezuelan borderland: Geological Society of America Bulletin, v. 86, no. 2, p. 213-226.

Silver, E. A., Case, J. E., and Tagg, A. R., 1972, Acoustic reflection profiles, Venezuela continental borderland: U.S. Geol. Surv. .

Smith, J. R., Malahoff, A., and Shor, A. N., 1999, Submarine geology of the Hilina

    slump and morpho-structural evolution of Kilauea volcano, Hawaii: Journal of

    Volcanology and Geothermal Research, v. 94, no. 1–4, p. 59-88.

Soest, R. W. M. V., Meesters, E. H. W. G., and Becking, L. E., 2014, Deep-water

    sponges (Porifera) from Bonaire and Klein Curaçao, Southern Caribbean:

    Zootaxa, v. 3878, no. 5, p. 401-443.

Spikings, R., Cochrane, R., Villagomez, D., Van der Lelij, R., Vallejo, C., Winkler, W.,

    and Beate, B., 2015, The geological history of northwestern South America: from

    Pangaea to the early collision of the Caribbean Large Igneous Province (290–75

    Ma): Gondwana Research, v. 27, no. 1, p. 95-139.

Sulaica, J. L., 2015, Facies Distribution and Paleogeographic Evolution of Neogene

    Carbonates in Bonaire, Netherlands Antilles [M.S.: Texas A&M University.

Symithe, S., Calais, E., de Chabalier, J. B., Robertson, R., and Higgins, M., 2015,

    Current block motions and strain accumulation on active faults in the Caribbean:

    Journal of Geophysical Research: Solid Earth, v. 120, no. 5, p. 3748-3774.

Thompson, P. M. E., Kempton, P. D., White, R. V., Saunders, A. D., Kerr, A. C.,

    Tarney, J., and Pringle, M. S., 2004, Elemental, Hf–Nd isotopic and

    geochronological constraints on an island arc sequence associated with the

    Cretaceous Caribbean plateau: Bonaire, Dutch Antilles: Lithos, v. 74, no. 1–2, p.

    91-116.

Trenkamp, R., Kellog, J., Freymueller, J., and Mora, H., 2002, Wide Plate Margin

    Deformation, Southern Central America and Northwestern South America,

CASA GPS Observations.: Journal of South American Earth Sciences, v. 15, p. 157-151.

Van der Lelij, R., Spikings, R. A., Kerr, A. C., Kounov, A., Cosca, M., Chew, D., and Villagomez, D., 2010, Thermochronology and tectonics of the Leeward Antilles: Evolution of the southern Caribbean Plate boundary zone: Tectonics, v. 29, no. 6, p. 1-30.

Van Duyl, F. C., 1985, Atlas of the living reefs of Curaçao and Bonaire (Netherlands Antilles) Utrecht, Netherlands Foundation for Scientific Research in Surinam and the Netherlands Antilles, Uitgaven van de Natuurwetenschappelijke Studiekring voor Suriname en de Nederlandse Antillen, v. 117.

Weber, J. C., Dixon, T. H., DeMets, C., Ambeh, W. B., Jansma, P., Mattioli, G., Saleh, J., Sella, G., Bilham, R., and Perez, O., 2001, GPS estimate of relative motion between the Caribbean and South American plates, and geologic implications for Trinidad and Venezuela: Geology [Boulder], v. 29, no. 1, p. 75-78.

Whattam, S. A., and Stern, R. J., 2015, Late Cretaceous plume-induced subduction initiation along the southern margin of the Caribbean and NW South America: The first documented example with implications for the onset of plate tectonics: Gondwana Research, v. 27, no. 1, p. 38-63.

Wright, J. E., and Wyld, S. J., 2011, Late Cretaceous subduction initiation on the eastern margin of the Caribbean-Colombian Oceanic Plateau: One Great Arc of the Caribbean (?): Geosphere, v. 7, no. 2, p. 468-493.

Yilmaz, Ö., 2001, Seismic Data Analysis, Society of Exploration Geophysicists,

   Investigations in Geophysics, 2065 p.:

Zapata, S., Cardona, A., Montes, C., Valencia, V., Vervoort, J., and Reiners, P., 2014,

   Provenance of the Eocene Soebi Blanco formation, Bonaire, Leeward Antilles:

   Correlations with post-Eocene tectonic evolution of northern South America:

   Journal of South American Earth Sciences, v. 52, p. 179-193.
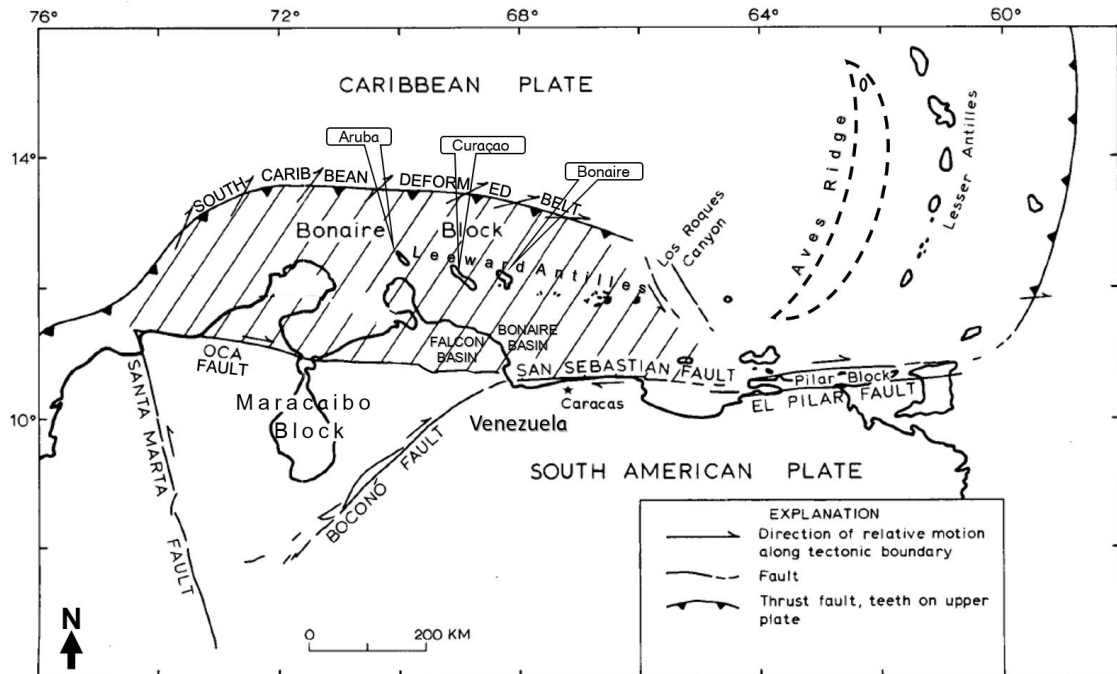
Figure 1: Regional map showing the southern Caribbean plate margin. Shaded area defined by dashed lines marks the geographical extent of the 'Bonaire Block.' The Falcon and Bonaire basins are labeled at their approximate geographic location. The ABCs (Aruba, Bonaire, Curaçao) are denoted in callouts. The Aves Ridge is defined by the dashed crescent shape (modified from Silver et al., 1975).
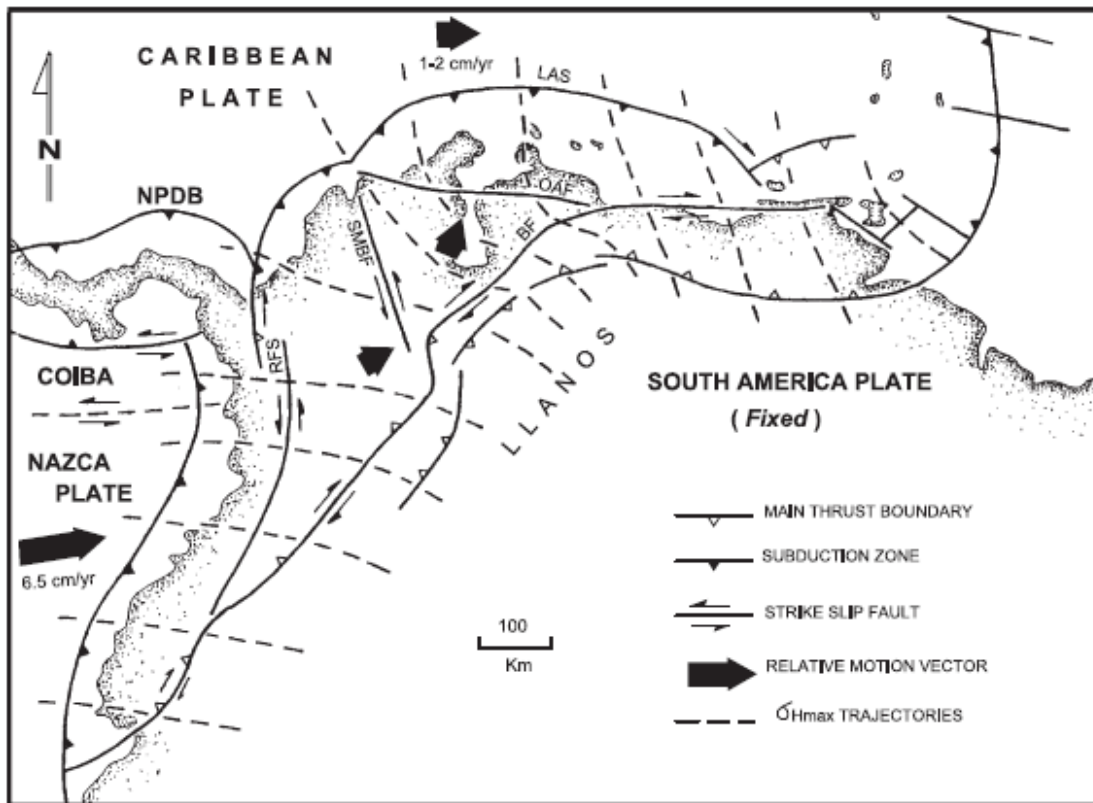
Figure 2: Maximum horizontal stress trajectories for northern South America. Legend: BF: Boncó Fault, LAS: Leeward Antilles Subductin (referred to in this paper as the SCDB-South Caribbean Deformation Belt), OAF: Oca-Ancón Fault (Audemard, 2005).
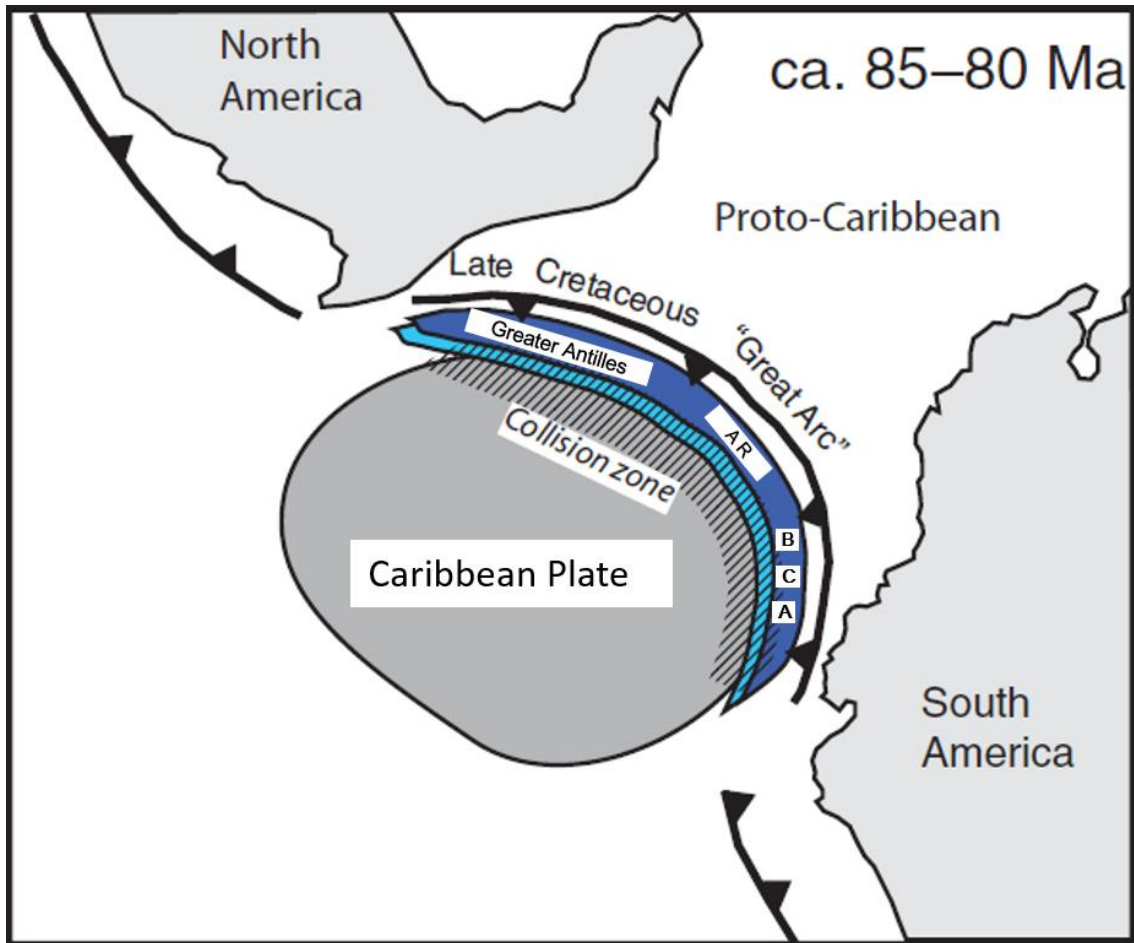
Figure 3: Tectonic model showing the 'Great Arc of the Caribbean' on the former leading edge of the Caribbean plate as the plate migrated east from the Pacific during the late Cretaceous. The ABCs (Aruba, Bonaire, Curaçao), Aves Ridge, and Greater Antilles are depicted as part of the continuous and single Great Arc of the Caribbean. Abbreviations as follows: AR-Aves Ridge; B-Bonaire; C-Curaçao; A-Aruba (modified from Wright and Wyld, 2011).
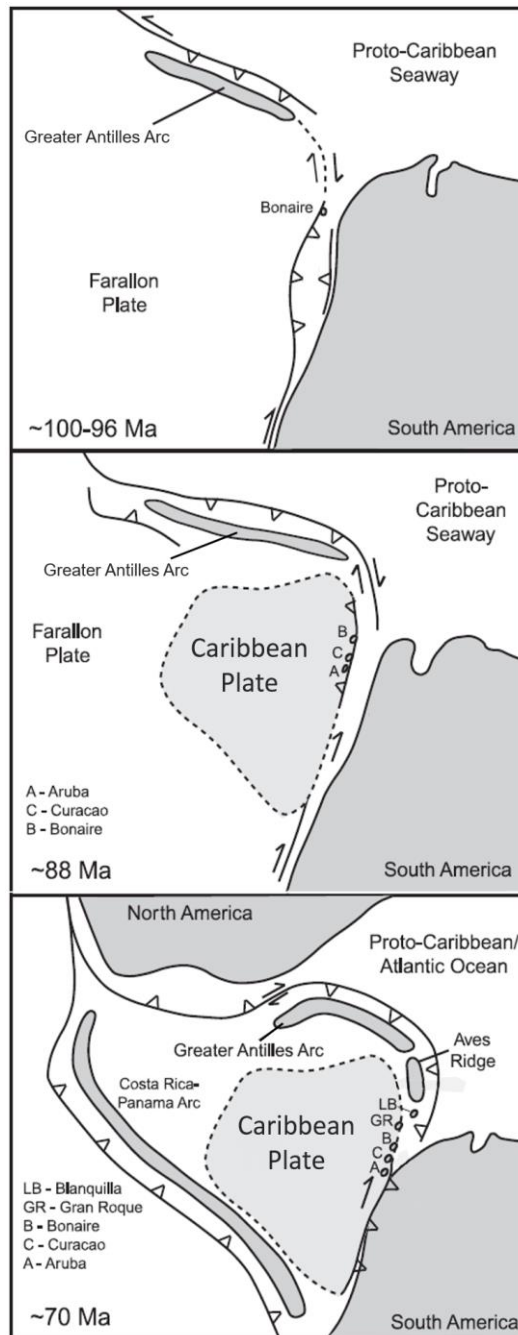
Figure 4: Regional maps explaining the evolution of Caribbean tectonics in multiple distinct terranes rather than a single Great Arc of the Caribbean: (a) ~100 Ma, Bonaire as part of a separate smaller arc; (b) ~88 Ma emergence of the Caribbean plate and formation of Aruba and Curaçao; (c) ~70 Ma formation of the Aves Ridge (modified from Neill et al., 2011).
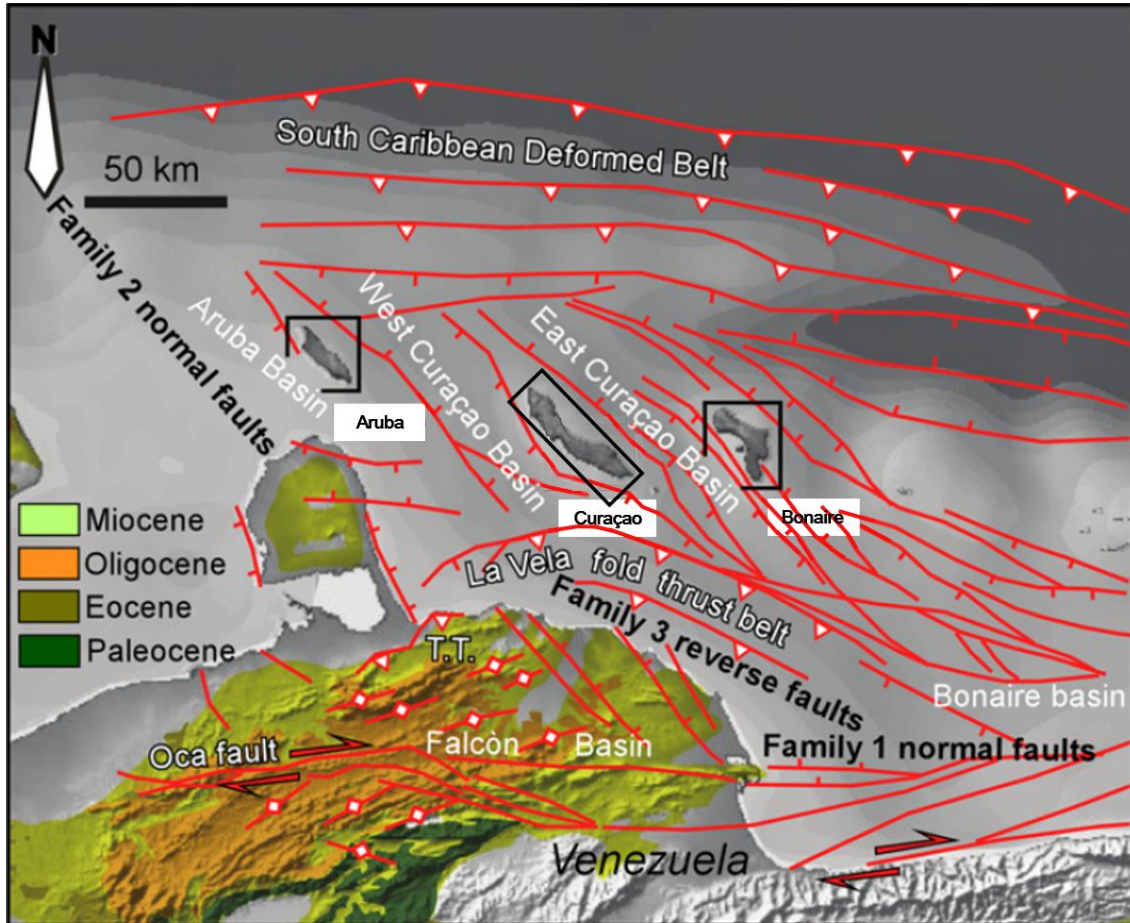
Figure 5: Tectonic map of the ABCs (Aruba, Bonaire, Curaçao) showing the regional tectonic structures. The fault families identified by Gorney et al. (2007) have been labeled near and with the trend of the respective structures: Family 1) E-W-striking Eocene-Oligocene normal faults; Family 2) NW-striking Oligocene-Holocene normal faults; Family 3) WNW-striking middle Miocene-Holocene reverse faults (modified from Hippolyte and Mann, 2011). The Falcon basin is the western termination of the offshore Bonaire basin, and both are labeled in their approximate geographic locations. The reverse faulting at the South Caribbean Deformed Belt has been ongoing since the middle Eocene (Kroehler et al., 2011).
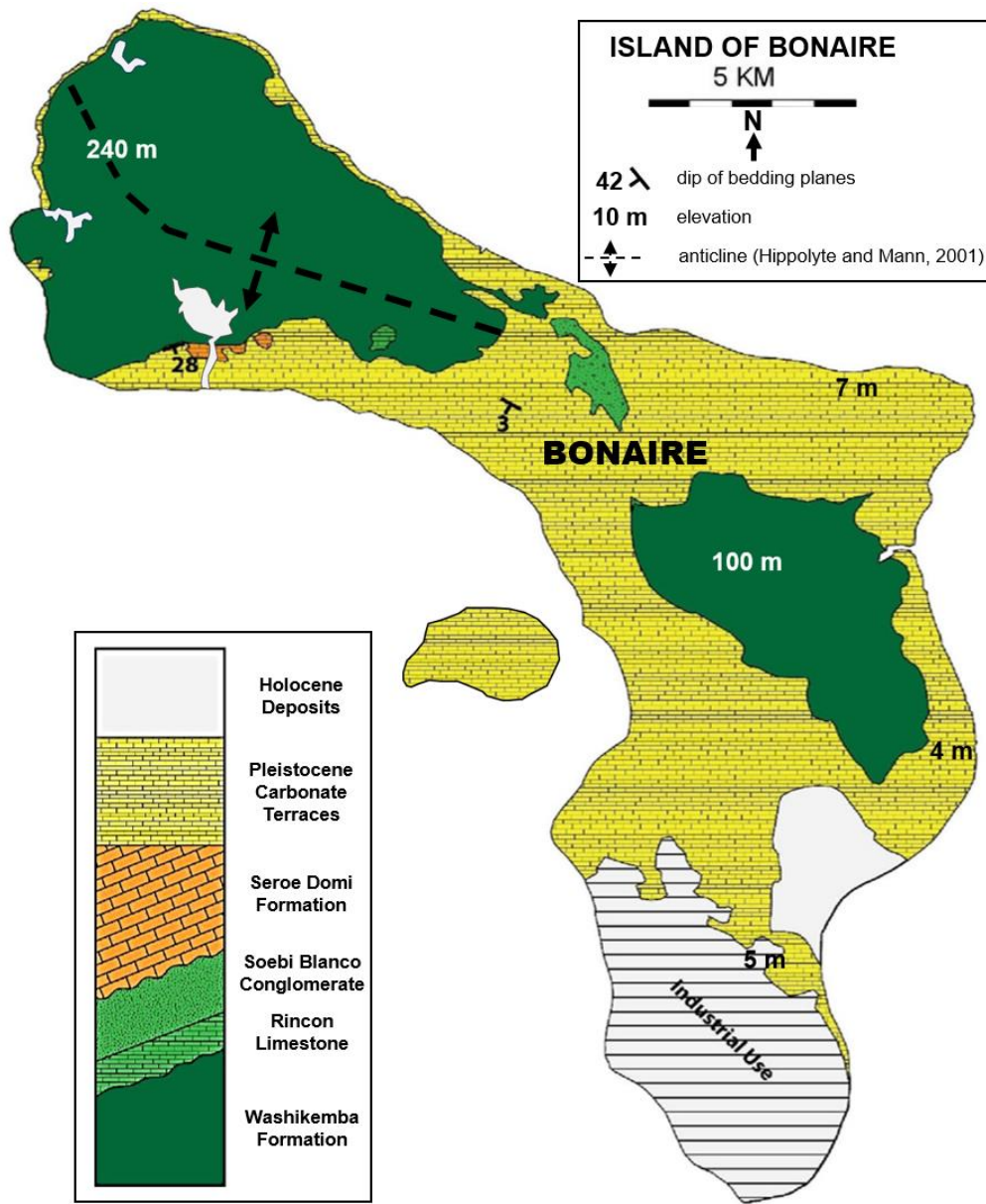
Figure 6: Geologic sketch of Bonaire with simplified stratigraphic section and mapping by De Buisonjé (1974) and Sulaica (2015). The NW-SE trending anticline interpreted by Hippolyte and Mann (2011) is plotted in the north of the island (modified from De Buisonjé, 1974; Hippolyte and Mann, 2011; Sulaica, 2015).
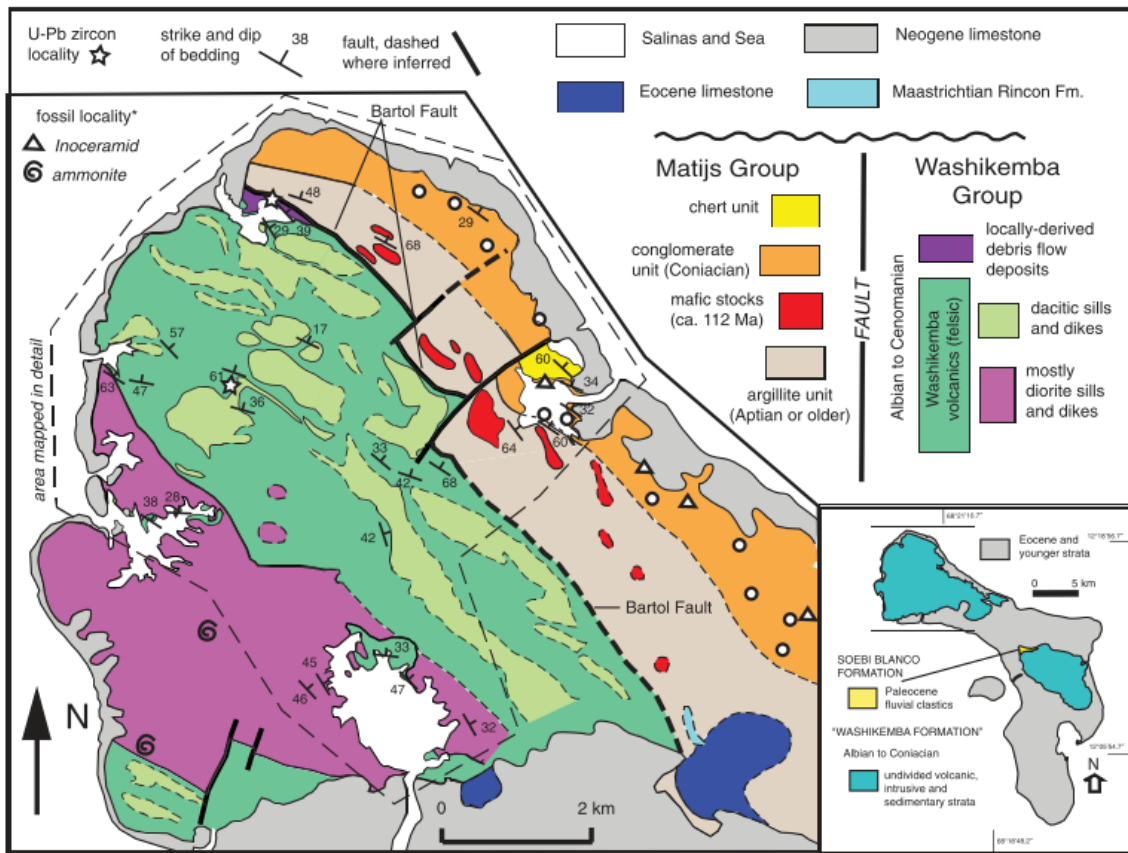
Figure 7: Reinterpretion and mapping of northern Bonaire showing the proposed Bartol Fault, separating the Washikemba formation into the Washikemba Group and Matjis Group. The Washikemba Group and the Matjis Group partially overlap in age, with the Matjis Group containing the oldest and youngest rock ages. Though the sense of offset along the Bartol fault has yet to be determined, the Matjis Group has been mapped on the northeast side of the fault, while the Washikemba Group has been mapped on the southwest side of the fault. Inset shows generalized geology of the island of Bonaire (Wright &Wyld, 2011).

Figure 8: Bathymetry map showing major structural features interpreted offshore of the ABCs (Aruba, Bonaire, Curaçao), including the NW-SE trending anticline extending offshore north of the ABCs (modified from Silver et al., 1975).

66
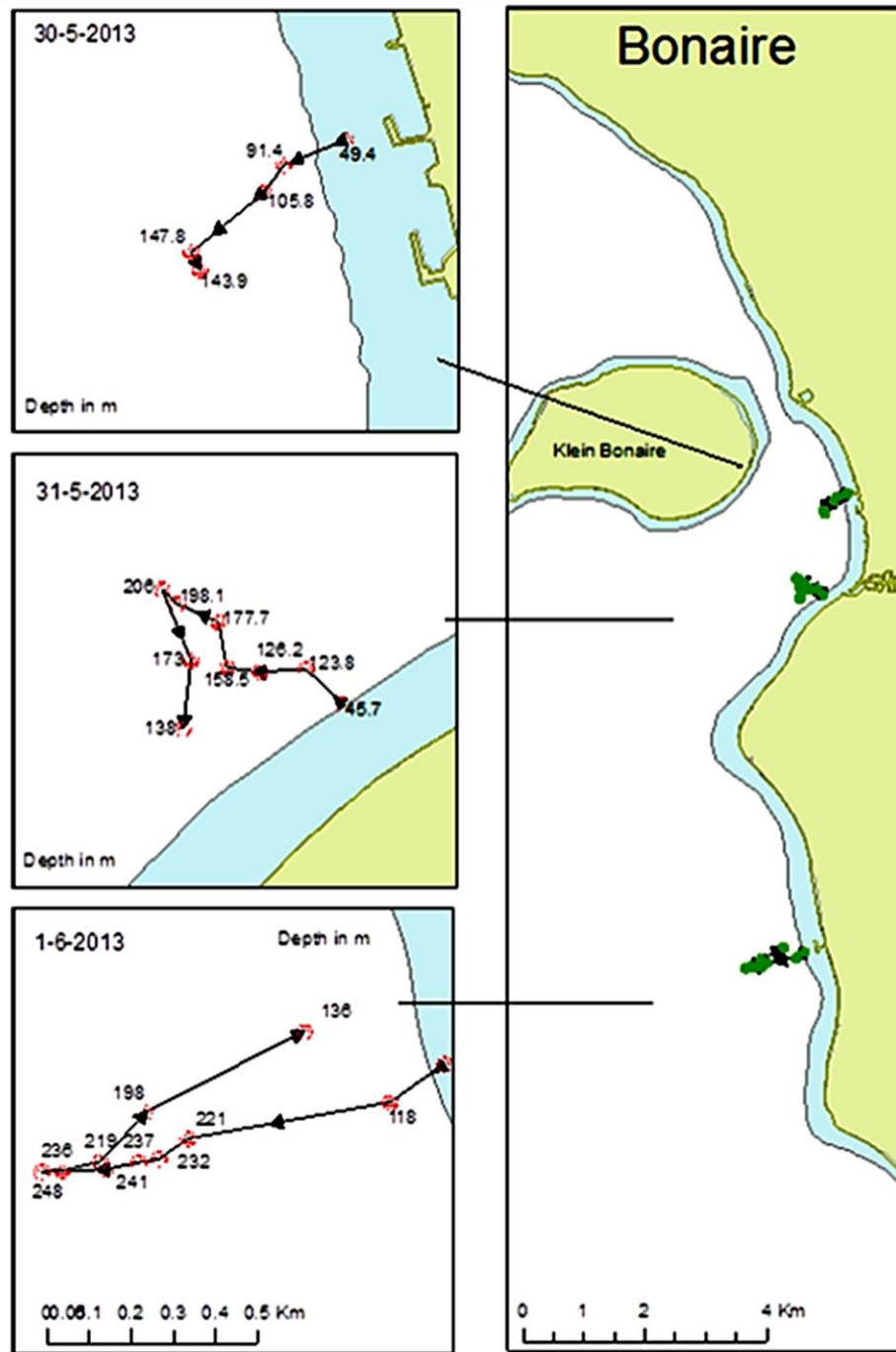
Figure 9: Map showing the detailed dive locations and track lines of the submarine dives from Soest et al. (2014). The arrows on the track lines the left panel indicate dive direction, and the numbers next to the track lines (modified from Soest et al., 2014).

Figure 10: Limestone rock collected from the seafloor substrate at a depth of ~238 m off the southern coast of Bonaire, with a seafoam green colored sponge located in the center of the rock sample (Soest et al., 2014).
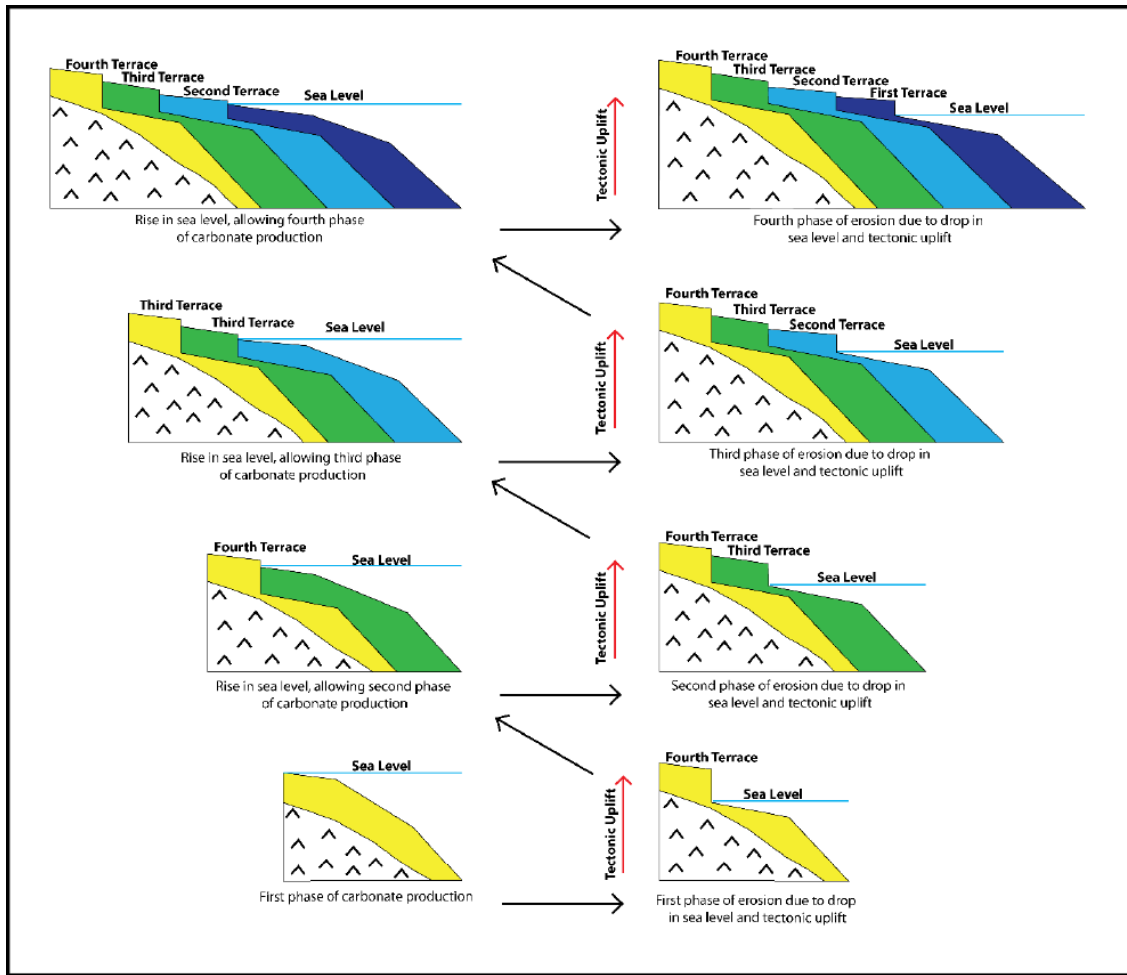
Figure 11: Schematic cross-section of Bonaire showing the proposed offlapping pattern of Bonaire's Pleistocene carbonate terraces (Sulaica, 2015).
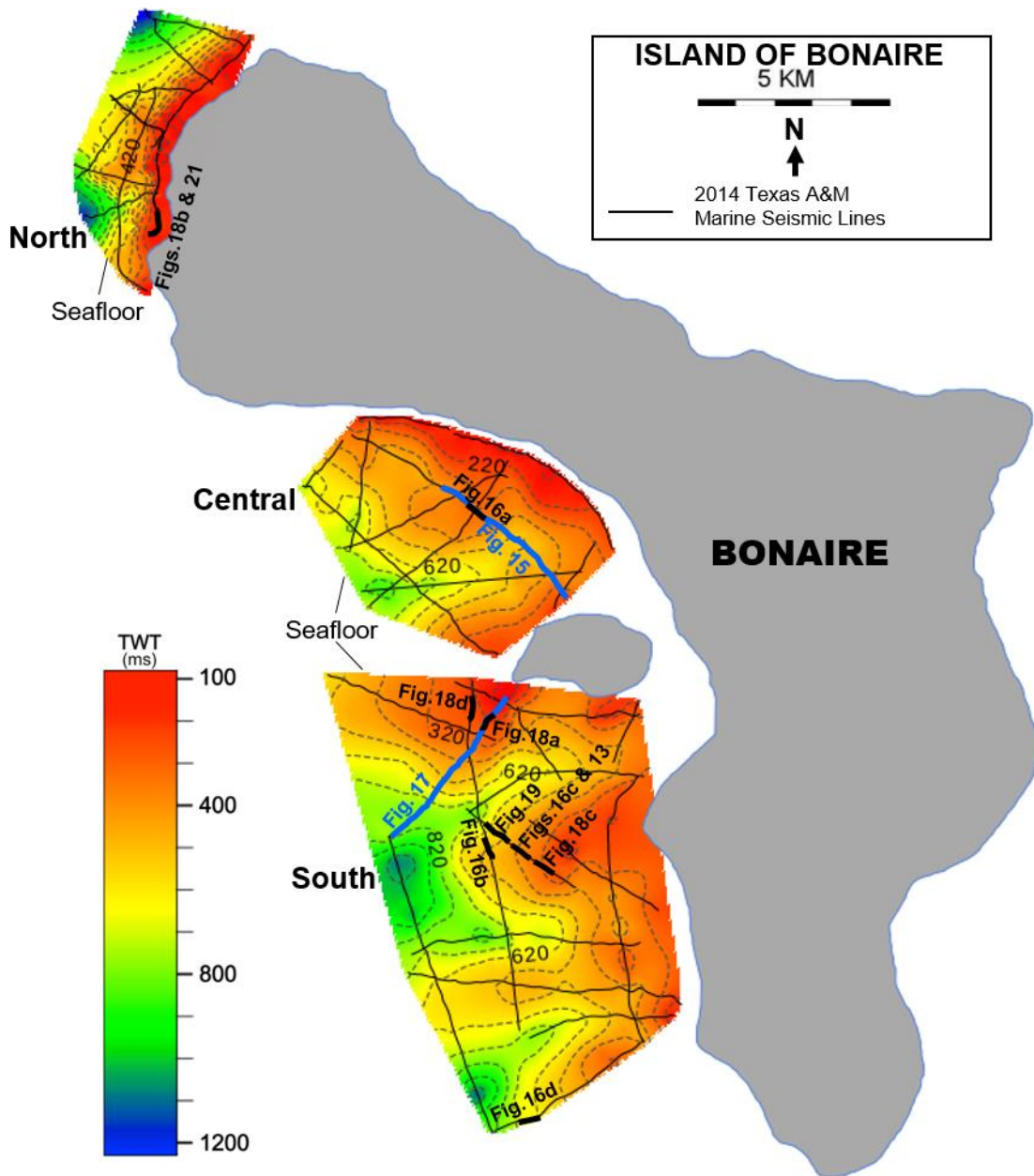
Figure 12: Map showing the location of gridded seafloor surface of the three study regions. The light gray dashed lines in the grids represent 100 (ms) contour interval. The dark skinny lines perpendicular to the seafloor contours mark the location of the seismic lines from this study. The location of seismic profiles referenced in this study are bolded and labeled on the seismic lines.
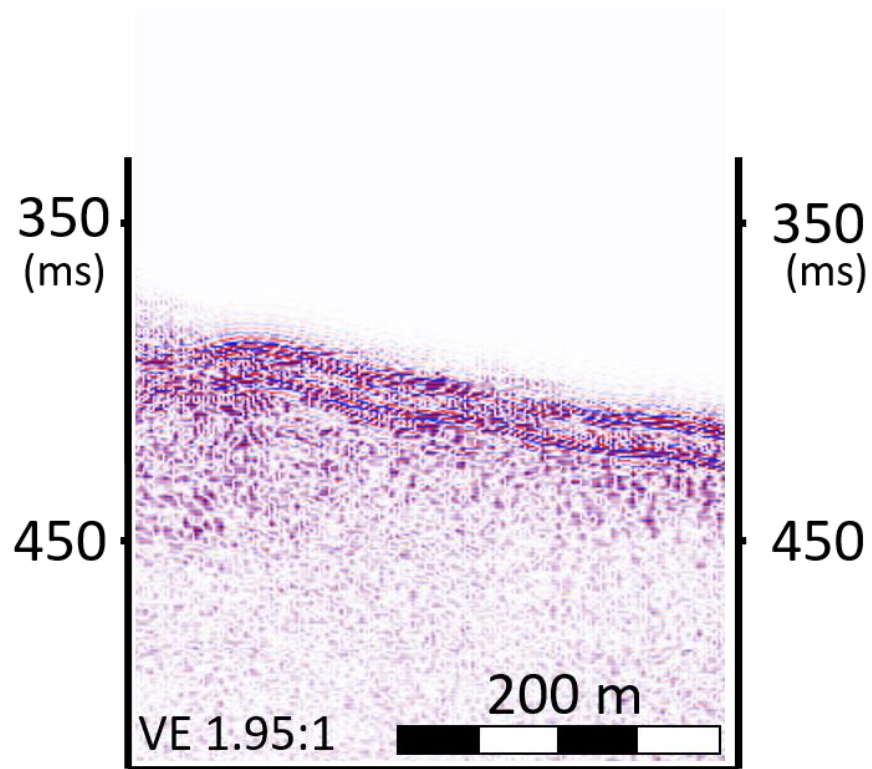
Figure 13: Seismic reflection profile showing the seismic response of the hard bottom seafloor typical in the majority of our data. Vertical exaggeration (VE) based on an assumed 3500 m/s seafloor velocity. Location of seismic reflection profile shown in Fig. 12.
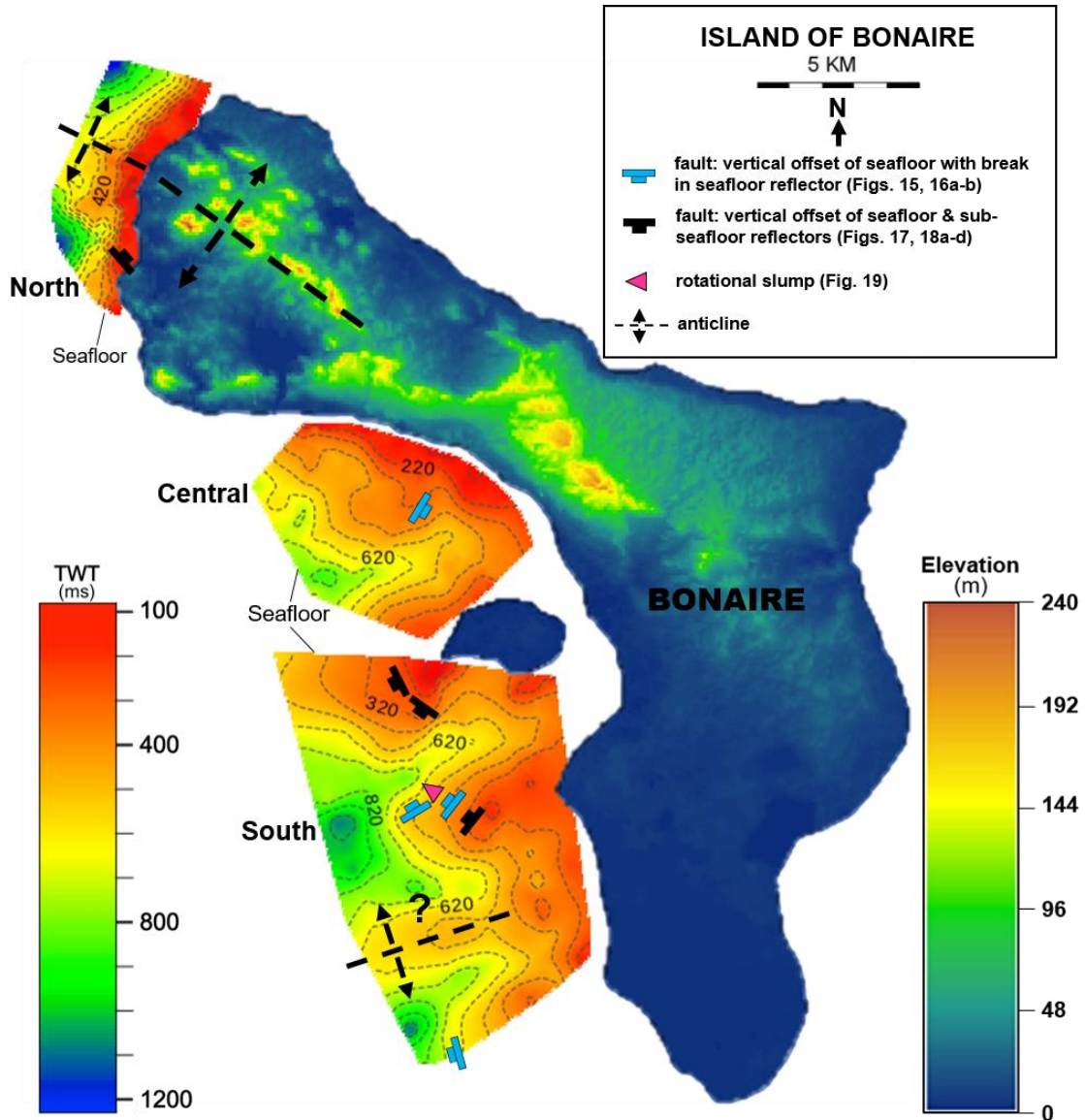
Figure 14: Digital elevation model of Bonaire and time structure map of the seafloor. The color bar on the right corresponds to the digital elevation model of Bonaire and indicates elevation in meters. The color bar on the left corresponds to the time structure maps of the seafloor off the west coast of Bonaire and indicates seismic two-way-travel time in milliseconds. The light gray dashed lines in the time structure maps of the seafloor represent 100 ms contour interval.
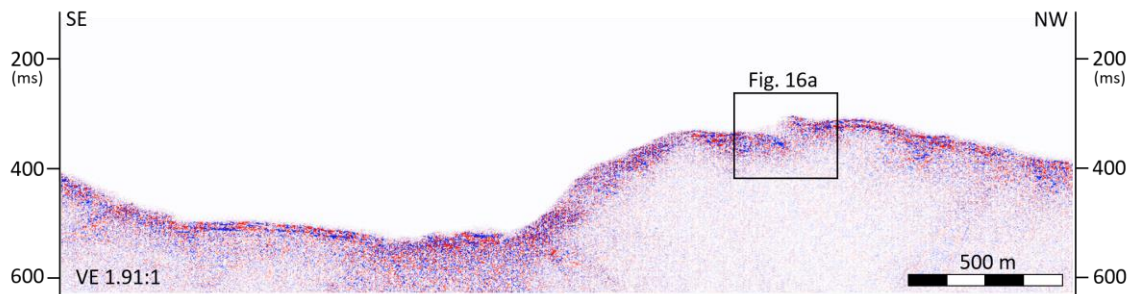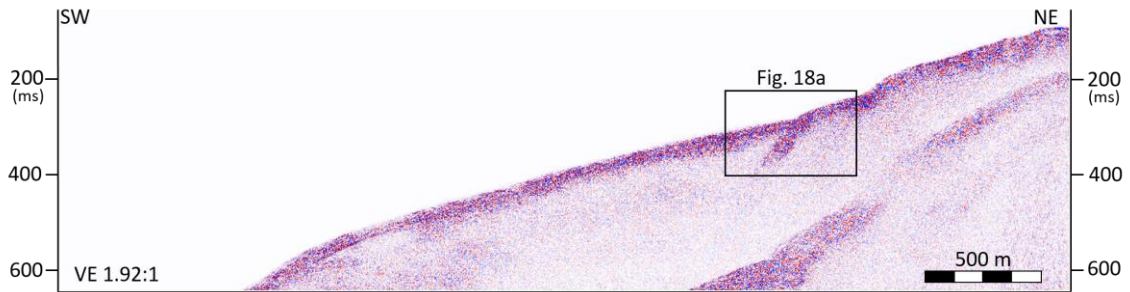
Figure 15: Seismic profile showing the type example for the seafloor discontinuities classified in our data as 'vertical offset with a discernable break in the seafloor reflector.' Vertical exaggeration (VE) based on an assumed 3500 m/s seafloor velocity. Location of seismic profile shown in Fig. 12. Interpreted discontinuity shown in Fig. 16a; inset black box denotes extent of seismic profile shown in Fig. 16a.
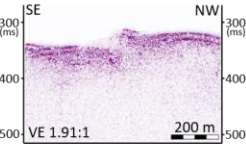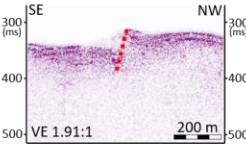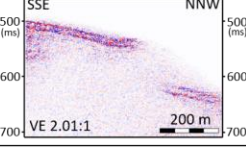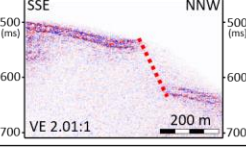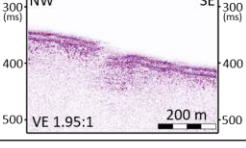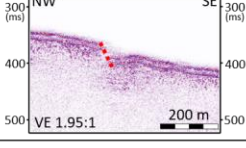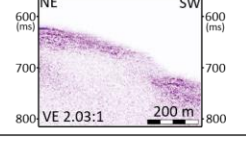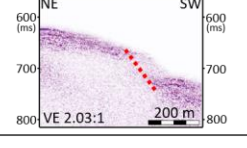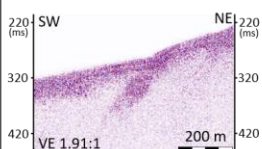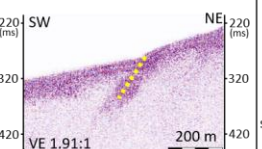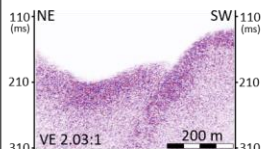
	Un-interpreted Discontinuity	Fault Interpretation	Reflector Discontinuity Characteristic	Vertical Seafloor Offset: TWT (ms)	Horizontal Offset (m)	Dip Direction	Strike
A			Vertical offset with a discernable break in the seafloor reflector	17	119	SE	NE-SW
B			Vertical offset with a discernable break in the seafloor reflector	89	146	NNW	WSW-ENE
C			Vertical offset with a discernable break in the seafloor reflector	27	60	NW	NE-SW
D			Vertical offset with a discernable break in the seafloor reflector	68	153	SW	NW-SE

Figure 16: Seismic profiles of all discontinuities classified in our data as 'vertical offset with a discernable break in the seafloor reflector.' Red dashed line represents normal fault. Vertical exaggeration (VE) based on an assumed 3500 m/s seafloor velocity. Location of seismic profiles shown in Fig. 12.

Figure 17: Seismic profile showing the type example for the seafloor discontinuities classified in our data as 'vertical offset with or without a discernable break in the seafloor reflector and sub-vertical reflectors extending into the sub-surface from the seafloor.' Vertical exaggeration (VE) based on an assumed 3500 m/s seafloor velocity. Location of seismic profile shown in Fig. 12. Interpreted discontinuity shown in Fig. 18a; inset black box denotes extent of seismic profile shown in Fig. 18a.
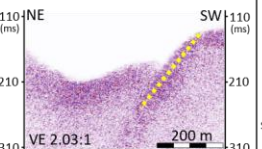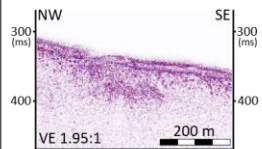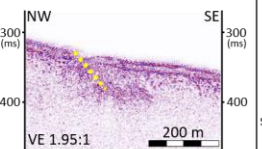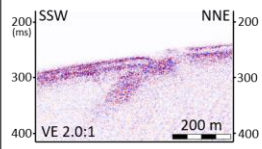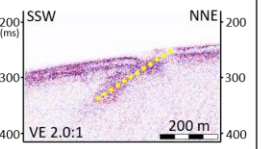
	Un-interpreted Discontinuity	Fault Interpretation	Reflector Discontinuity Characteristic	Vertical Seafloor Offset: TWT (ms)	Horizontal Offset (m)	Dip Direction	Strike
A			Vertical offset without a discernable break in the seafloor reflector and sub-vertical reflectors extending into the sub-surface from the seafloor	28	31.25	SW	NW-SE
B			Vertical offset with a discernable break in the seafloor reflector and sub-vertical reflectors extending into the sub-surface from the seafloor	48	172	NE	NW-SE
C			Vertical offset without a discernable break in the seafloor reflector and sub-vertical reflectors extending into the sub-surface from the seafloor	10	28	NW	NE-SW
D			Vertical offset with a discernable break in the seafloor reflector and sub-vertical reflectors extending into the sub-surface from the seafloor	20	28	SW	NW-SE

Figure 18: Seismic profiles of all discontinuities classified in our data as 'vertical offset with or without a discernable break in the seafloor reflector and sub-vertical reflectors extending into the sub-surface from the seafloor.' Yellow dashed line represents normal fault. Vertical exaggeration (VE) based on an assumed 3500 m/s seafloor velocity. Location of seismic profiles shown in Fig. 12.
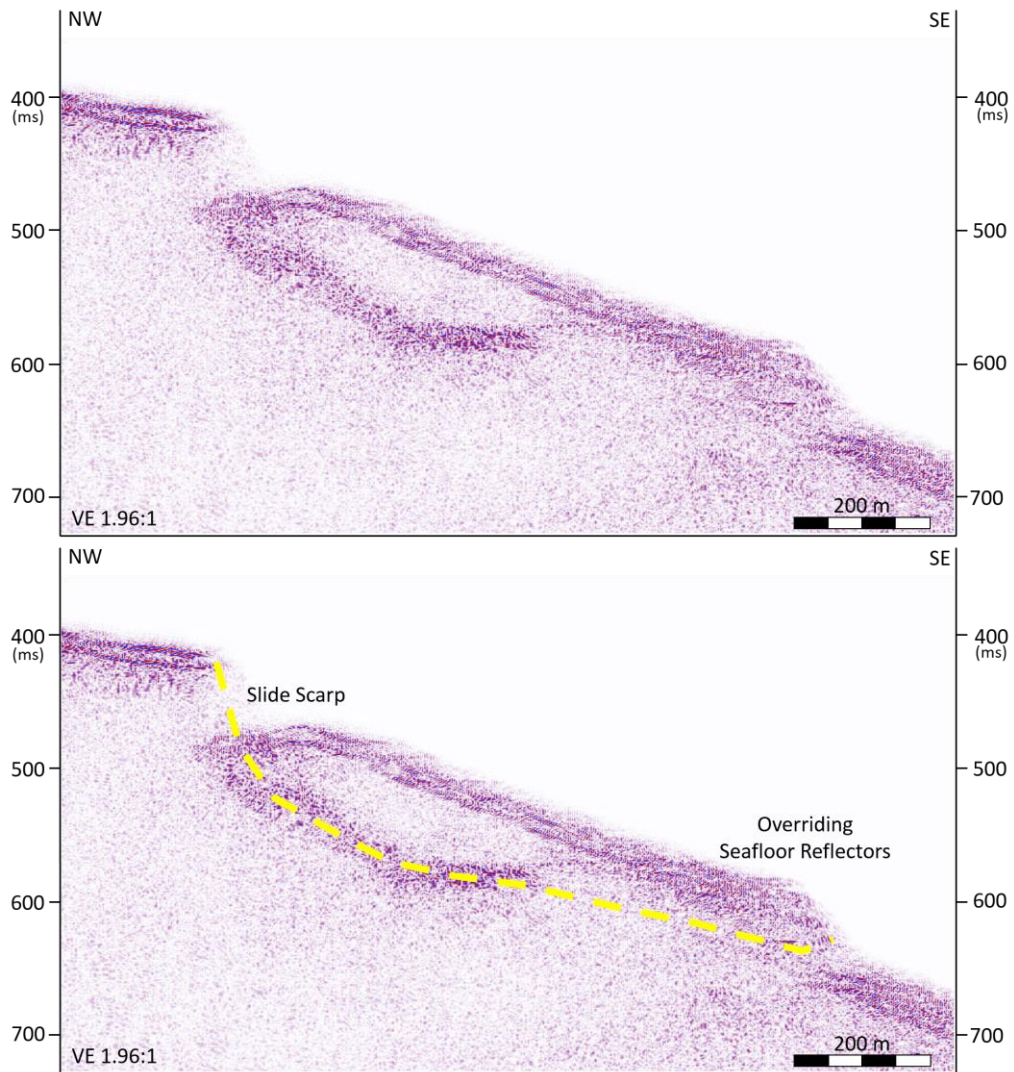
Figure 19: Seismic profile of the discontinuity we classify in our data as a 'discernable upslope break and offset and overriding seafloor reflectors downslope.' Yellow dashed line represents the slide plane of interpreted rotational slump of the hard rock marine slope. Vertical exaggeration (VE) based on an assumed 3500 m/s seafloor velocity. Location of seismic profile shown in Fig. 12.
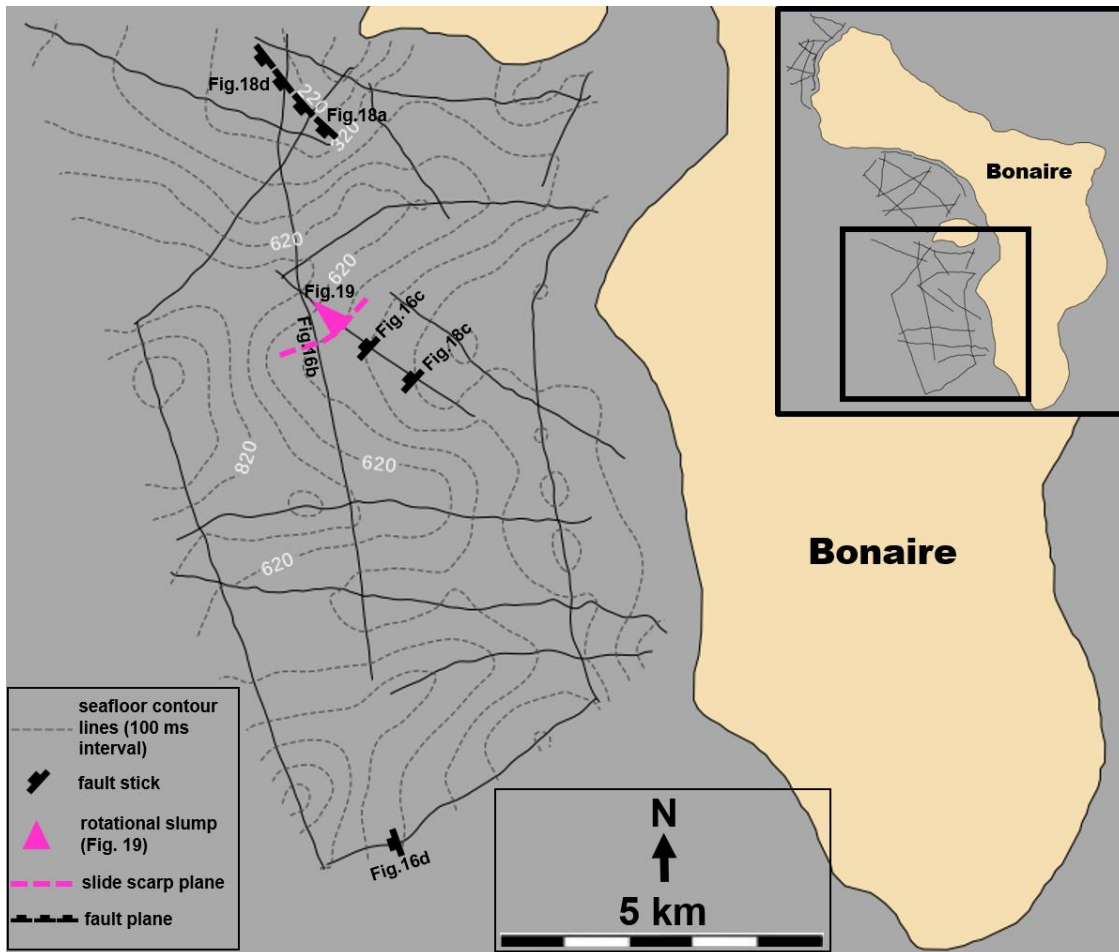
Figure 20: Zoomed in image of the south study region with structural features shown.
The structural features in Fig. 18a and 18d have been interpreted as part of the same
fault plane. The structural features in Fig.19 and Fig. 16b have been proposed to belong
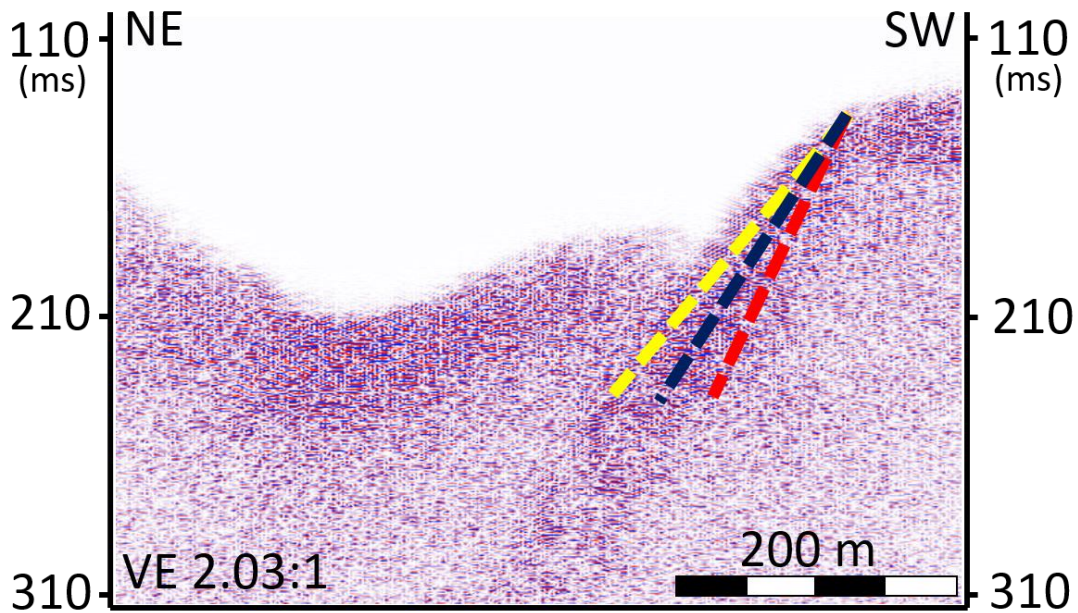to the same scarp plane.

Figure 21: Seismic profile showing that the sub-vertical reflectors in our data appear as wide reflectors with an unclear termination point, and at that the exact location and direction of the fault plane is unknown. To account for this unknown, we propose three varying fault plane locations within the sub-vertical reflectors to cover the possible direction and location the fault plane could occur. An example of three varying possible fault locations are plotted as dashed line is red, yellow, and blue. Vertical exaggeration (VE) based on an assumed 3500 m/s seafloor velocity. Location of seismic profile shown in Fig. 12.
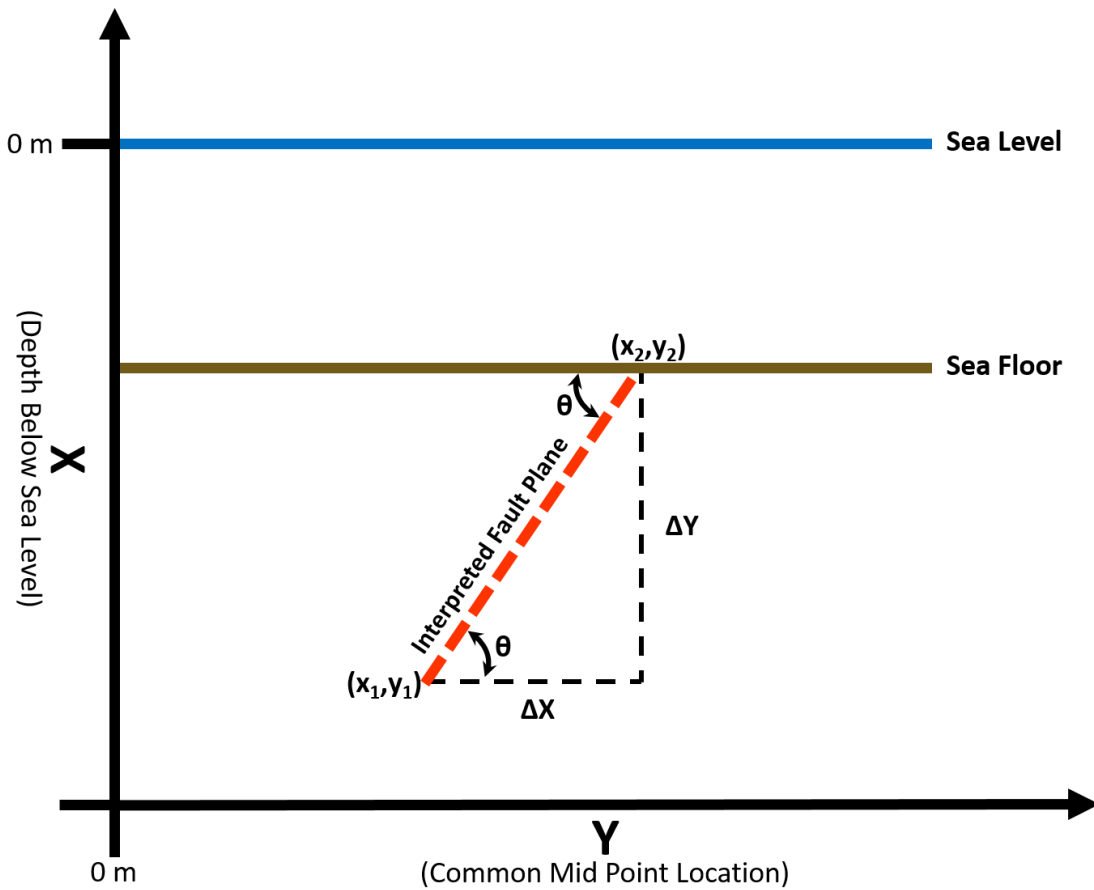
Figure 22: Schematic drawing used for fault plane estimation. The depth below sea level of the termination point of the fault plane is x_1, the CMP location of the termination point of the fault plane is y_1, the depth below sea level of the start point of the fault plane at the seafloor is x_2, and the CMP location of the start point of the fault plane at the seafloor is y_2. CMP location is a length in meters from the start of the seismic line. The slope of the fault plane is m.
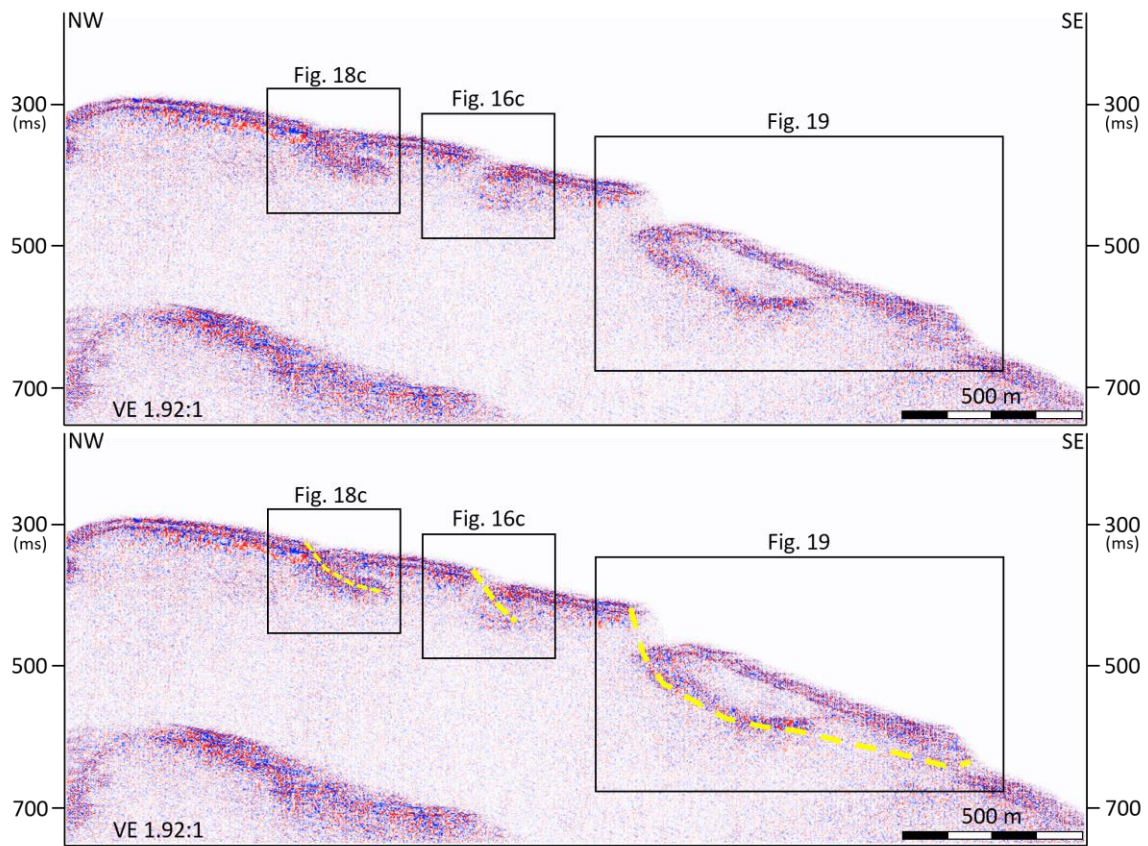
Figure 23: Seismic profile showing the relationship of Figs. 16c, 18c, and 19. We interpret that Fig. 19 is a rotational slump and that faults in Figs. 16c and 18c are related to the same process that influenced the landslide. Vertical exaggeration (VE) based on an assumed 3500 m/s seafloor velocity. Location of seismic profile shown in Fig. 12.

81

Medium Below Water Column	Velocity=v (km/s)	Density=ρ (g/cm^3)	Reflection Coefficient: R=$(v_2\rho_2-v_1\rho_1)/(v_2\rho_2+v_1\rho_1)$
Basalt[1]	5.9	3.1	0.831
Granite[2]	4.7	2.7	0.781
Limestone (high end value)[3]	5.5	2.7	0.812
Limestone (low end value)[3]	3.2	2.3	0.654
Calcareous Sediment (high end value)[4]	1.8	2.0	0.401
Calcareous Sediment (low end value)[4]	1.6	1.7	0.278

Table 1: Estimated velocity, density, and reflection coefficient values of the possible seafloor lithologies off Bonaire. 1. Hyndman and Drury (1976); 2. Barrett and Froggatt (1978); 3. Hamilton (1978) 4. Jackson and Richardson (2007)

Possible Seafloor Lithology	Lithology Velocity=v (km/s)	Minimum Vertical Resolution= ¼ v/f (m)
Basalt	5.9	2.46
Granite	4.7	1.96
Limestone (high end value)	5.5	2.29
Limestone (low end value)	3.2	1.33
Calcareous Sediment (high end value)	1.8	0.75
Calcareous Sediment (low end value)	1.6	0.67

Table 2: Possible vertical resolution of the seafloor off Bonaire based on a dominant survey frequency of 600 Hz. Velocity values are taken from Table 1.

Assumed Seafloor Lithology-Basalt: Velocity= v=5900 (m/s)					
x_1 (m)	y_1 (m)	x_2 (m)	y_2 (m)	m	θ
4112.50	-749.30	4225.00	-99.38	5.78	80.18°
4050.00	-749.30	4225.00	-99.38	3.71	74.93°
3996.88	-749.30	4225.00	-99.38	2.85	70.66°
Assumed Seafloor Lithology-Granite: Velocity= v=4700 (m/s)					
x_1 (m)	y_1 (m)	x_2 (m)	y_2 (m)	m	θ
4112.50	-596.90	4225.00	-99.38	4.42	77.26°
4050.00	-596.90	4225.00	-99.38	2.84	70.62°
3996.88	-596.90	4225.00	-99.38	2.18	65.37°
Assumed Seafloor Lithology-Limestone: Velocity= v=5500 (m/s)					
x_1 (m)	y_1 (m)	x_2 (m)	y_2 (m)	m	θ
4112.50	-698.50	4225.00	-99.38	5.33	79.37°
4050.00	-698.50	4225.00	-99.38	3.42	73.72°
3996.88	-698.50	4225.00	-99.38	2.63	69.15°
Assumed Seafloor Lithology-Limestone: Velocity= v=3200 (m/s)					
x_1 (m)	y_1 (m)	x_2 (m)	y_2 (m)	m	θ
4112.50	-406.40	4225.00	-99.38	2.73	69.88°
4050.00	-406.40	4225.00	-99.38	1.75	60.32°
3996.88	-406.40	4225.00	-99.38	1.35	53.39°

Table 3: Fault angle estimation of Fig. 18b. The depth below sea level of the termination point of the fault plane is x_1, the CMP location of the termination point of the fault plane is y_1, the depth below sea level of the start point of the fault plane at the seafloor is x_2, and the CMP location of the start point of the fault plane at the seafloor is y_2. CMP location is a length in meters from the start of the seismic line. The slope of the fault plane is m. The angle of the fault plane from horizontal, the seafloor, is θ and is measured in degrees. The assumed velocity values come from Table1. A visual representation of $x_1, x_2, y_1, y_2, m,$ and θ can be found in Fig. 22.

Assumed Seafloor Lithology-Basalt: Velocity= v=5900 (m/s)					
x_1 (m)	y_1 (m)	x_2 (m)	y_2 (m)	m	θ
4325.00	-555.76	4371.88	-207.33	7.43	82.34°
4300.00	-555.76	4371.88	-207.33	4.85	78.34°
4243.75	-555.76	4371.88	-207.33	2.72	69.81°
Assumed Seafloor Lithology-Granite: Velocity= v=4700 (m/s)					
x_1 (m)	y_1 (m)	x_2 (m)	y_2 (m)	m	θ
4325.00	-816.27	4371.88	-207.33	12.99	85.60°
4300.00	-816.27	4371.88	-207.33	8.47	83.27°
4243.75	-816.27	4371.88	-207.33	4.75	78.12°
Assumed Seafloor Lithology-Limestone: Velocity= v=5500 (m/s)					
x_1 (m)	y_1 (m)	x_2 (m)	y_2 (m)	m	θ
4325.00	-955.21	4371.88	-207.33	15.95	86.41°
4300.00	-955.21	4371.88	-207.33	10.41	84.51°
4243.75	-955.21	4371.88	-207.33	5.84	80.28°
Assumed Seafloor Lithology-Limestone: Velocity= v=3200 (m/s)					
x_1 (m)	y_1 (m)	x_2 (m)	y_2 (m)	m	θ
4325.00	-555.76	4371.88	-207.33	7.43	82.34°
4300.00	-555.76	4371.88	-207.33	4.85	78.34°
4243.75	-555.76	4371.88	-207.33	2.72	69.81°

Table 4: Fault angle estimation of Fig. 18a. The depth below sea level of the termination point of the fault plane is x_1, the CMP location of the termination point of the fault plane is y_1, the depth below sea level of the start point of the fault plane at the seafloor is x_2, and the CMP location of the start point of the fault plane at the seafloor is y_2. CMP location is a length in meters from the start of the seismic line. The slope of the fault plane is m. The angle of the fault plane from horizontal, the seafloor, is θ and is measured in degrees. The assumed velocity values come from Table1. A visual representation of $x_1, x_2, y_1, y_2, m,$ and θ can be found in Fig. 22.

This appendix presents the basic summary of the workflow used to process the 2014 Texas A&M marine seismic reflection data collected off the coast of Bonaire. Data was recoded in SEG-Y format and imported in to Paradigm for processing using the SEG-Y loader utility. The Paradigm SEG-Y loader utility imports the SEG-Y seismic data file into a Paradigm seismic database. Seismic data was imported one line at a time, and the lines were named according to the number in which they were acquired, e.g. the first line acquired is named 'line01'. Processing of the data was performed in the Paradigm Echos software. Figure A.1 shows the processing flow and processing jobs used for each line. Table A.1 lists the names we assigned the processing jobs and also lists the processing input and output file names. The processing jobs are presented in the numerical order in which they occurred, and are as follows (## is a place holder for the descriptive number in the line or water bottom name):

1. line##_1_geom.dat: Populates geometry tables in Echos database from specified information including data length, relative shot and receiver spacing, and receiver offset from source. Figure A.2 shows raw data.

2. line##_2_geomapplystatic.dat: Reads the SEG-Y seismic data file from the Paradigm seismic database into Echos and applies specified geometry information. Concurrently but apart from the job, spectral analysis of the seismic data frequency is performed to ascertain filtering needs (Fig. A.3). The job then applies a bandpass filter (300-400-1200-1400 Hz) to cut strong,

ubiquitous low-frequency discovered across the dataset. Additional notch

filtering at specific frequencies was needed for certain lines to reduce excess

noise. The job then shifts specific shot gathers down (104 ms) via static

correction to fix out of plane shots in certain lines.

3. line##_3_cdpsort.dat: Sorts the output from line##_2_geomapplystatic.dat

   job into CDP gathers.

4. line##_4_brutestack.dat: Generates a trace stack using the *normal* stacking

   algorithm in Echos with a 0.2 scalar. The water bottom (WB##) horizon was

   picked on this stack for use in subsequent jobs including deconvolution and

   muting (Fig. A.4).

5. line##_5a_decon.dat: Applies multichannel gapped predictive deconvolution:

   80 ms operator length, 1.5 gap length, and 0.1% white noise (Fig. A.5). Prior

   to deconvolution, shot gathers are shifted, via static shift, to the seafloor

   (WB## horizon) to eliminate the need to pick varying design and application

   windows for deconvolution operators. After deconvolution, the static shift is

   removed and an additional bandpass filter (300-400-1200-1400 Hz) is run.

6. line##_5b_sort.dat: Sorts the data output from line##_5a_decon.dat into CDP

   gathers and applies a spherical divergence or gain correction.

7. line##_6_veldef.dat: Opens interactive velocity picking tool for velocity

   analysis (Fig. A.6). Velocities were picked every 50 CDPs and saved to a

   velocity database (Fig. A.7).

8. line##_7_stack.dat: Applies normal move out (NMO) correction, velocity function top mute (mute##-for each respective line), and trace staking.

9. line##_8_fxmig.dat: Performs FK migration on the stacked data using the velocity picks from the database: lateral velocity smoothing=200 & vertical velocity smoothing=100. After migration, an additional water bottom mute is applied. Final processed shown in Figure A.8.
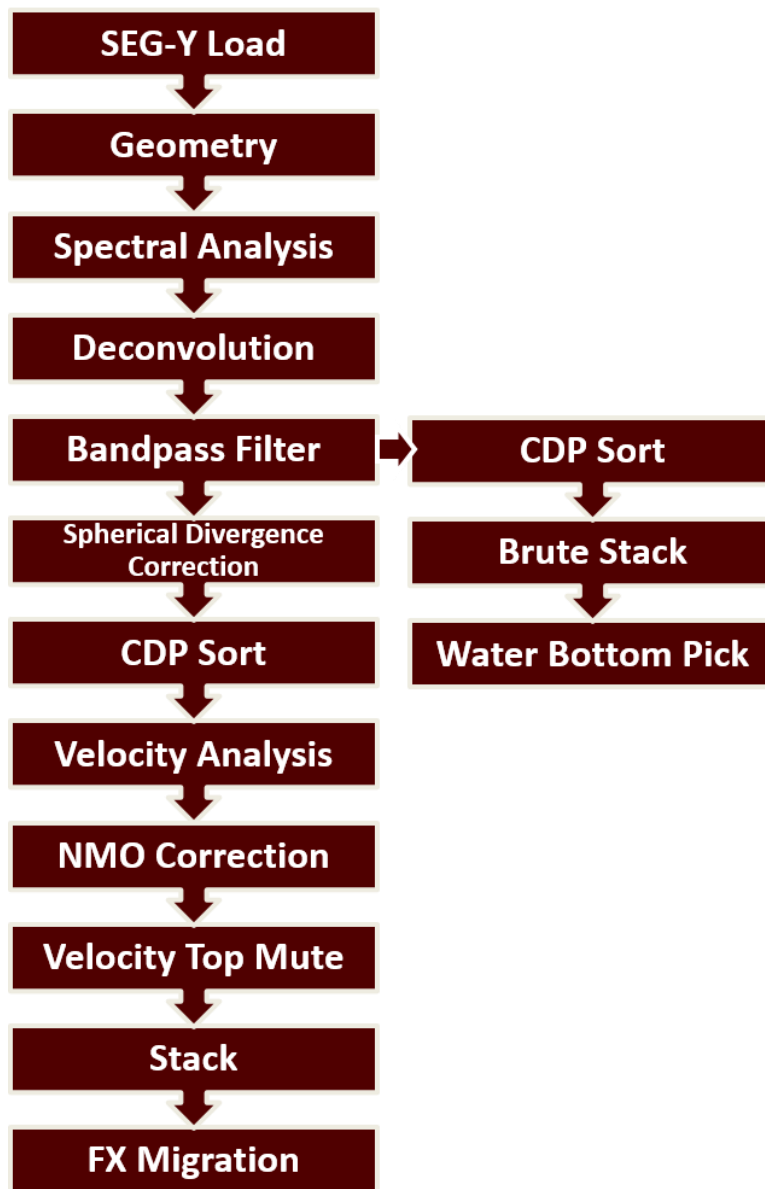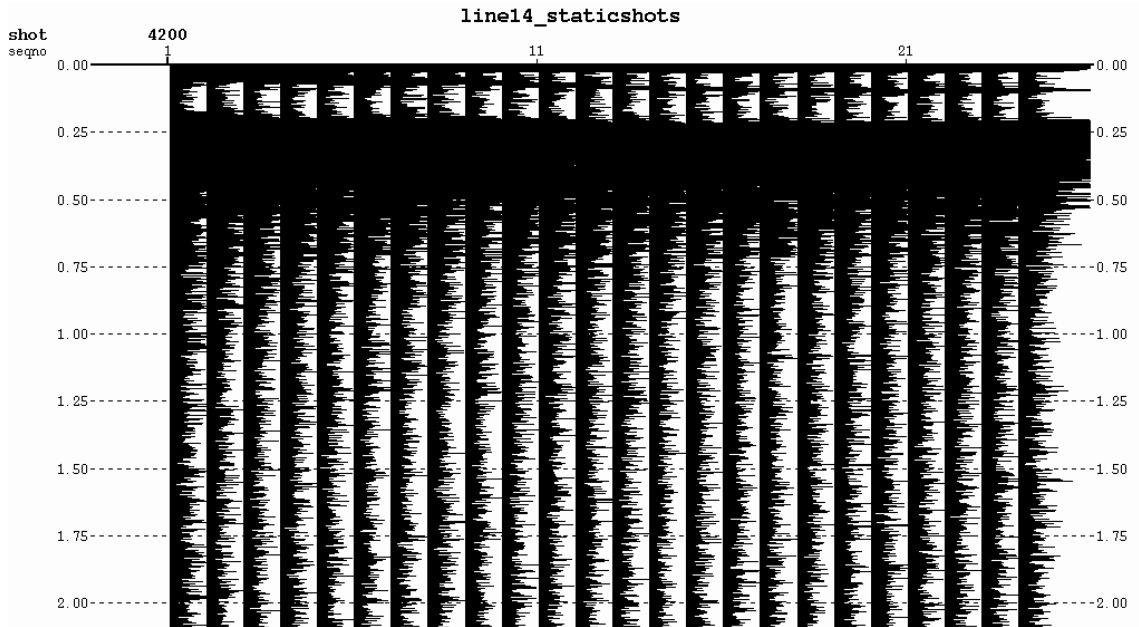
Figure A.1: Seismic processing workflow.

Figure A.2 Raw data of shot 4200 from line 14.
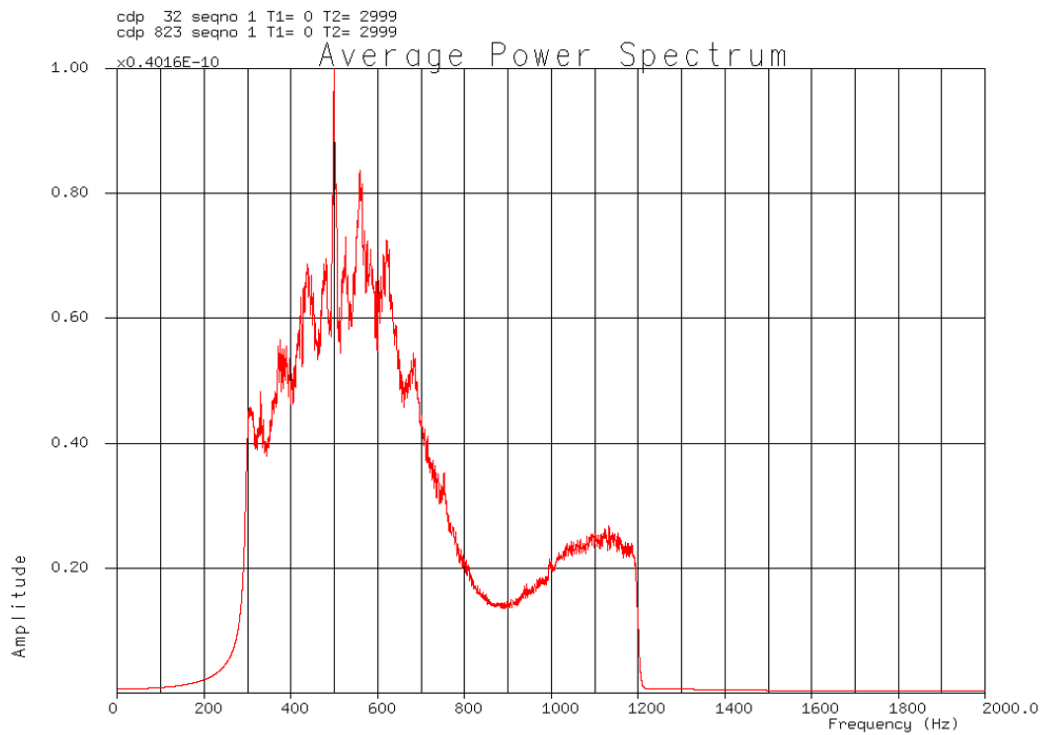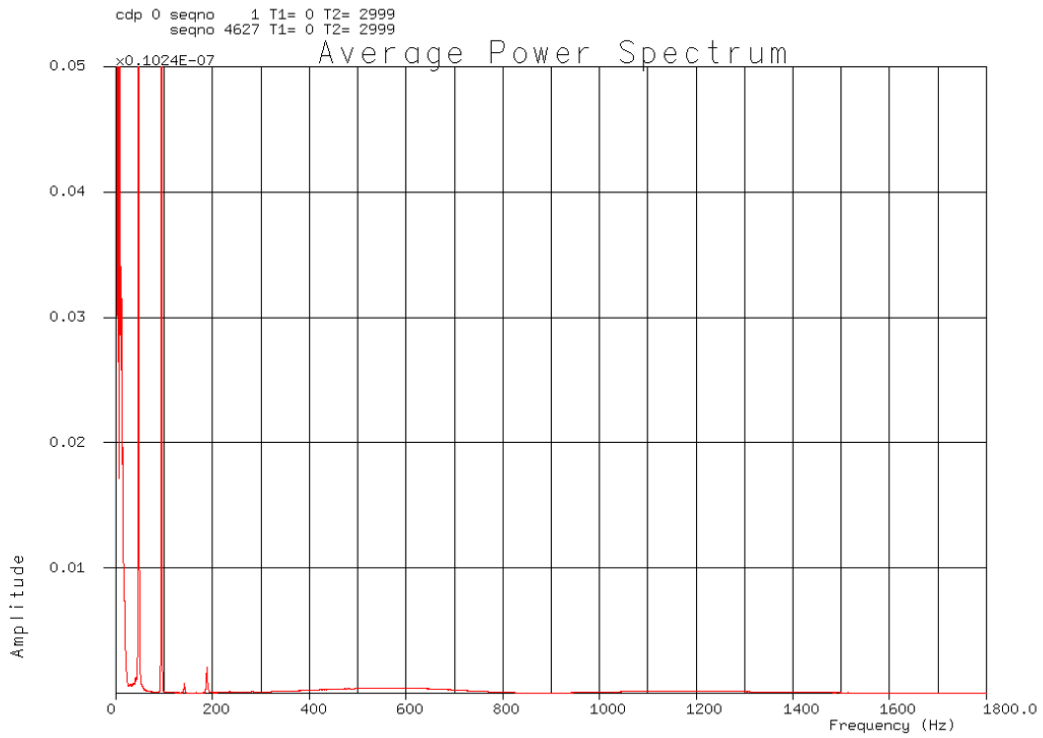
Figure A.3: Frequency analysis of the accumulation of all shot gathers in line 14 prior to any processing (top). Frequency analysis after applying bandpass filter (bottom).
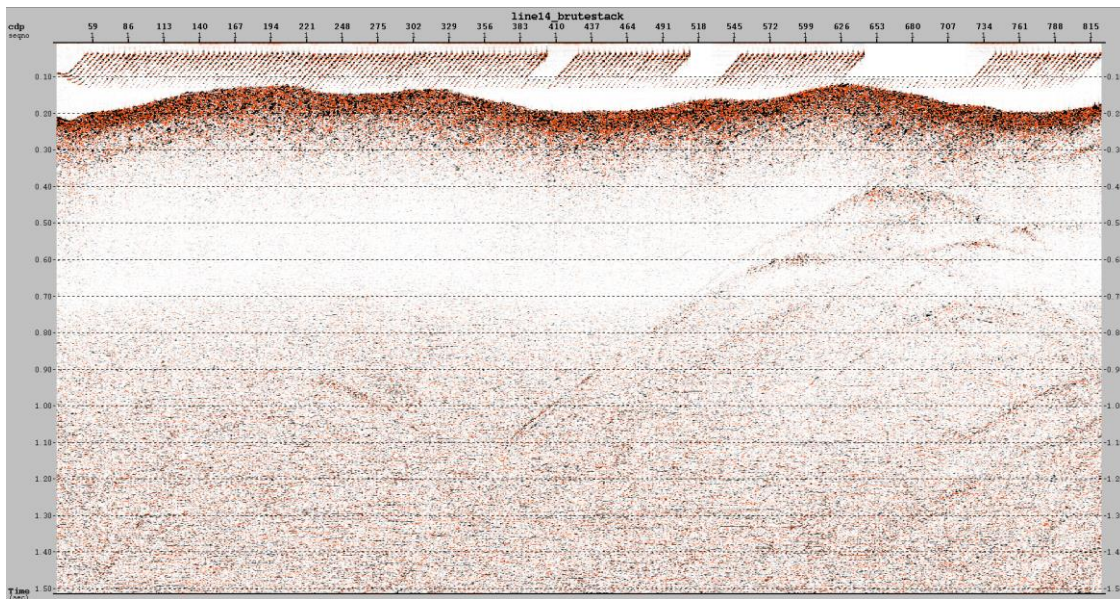
Figure A.4: Brute stack of line 14 with bandpass filter and prior to any further processing. Vertical Exaggeration is 1:1.
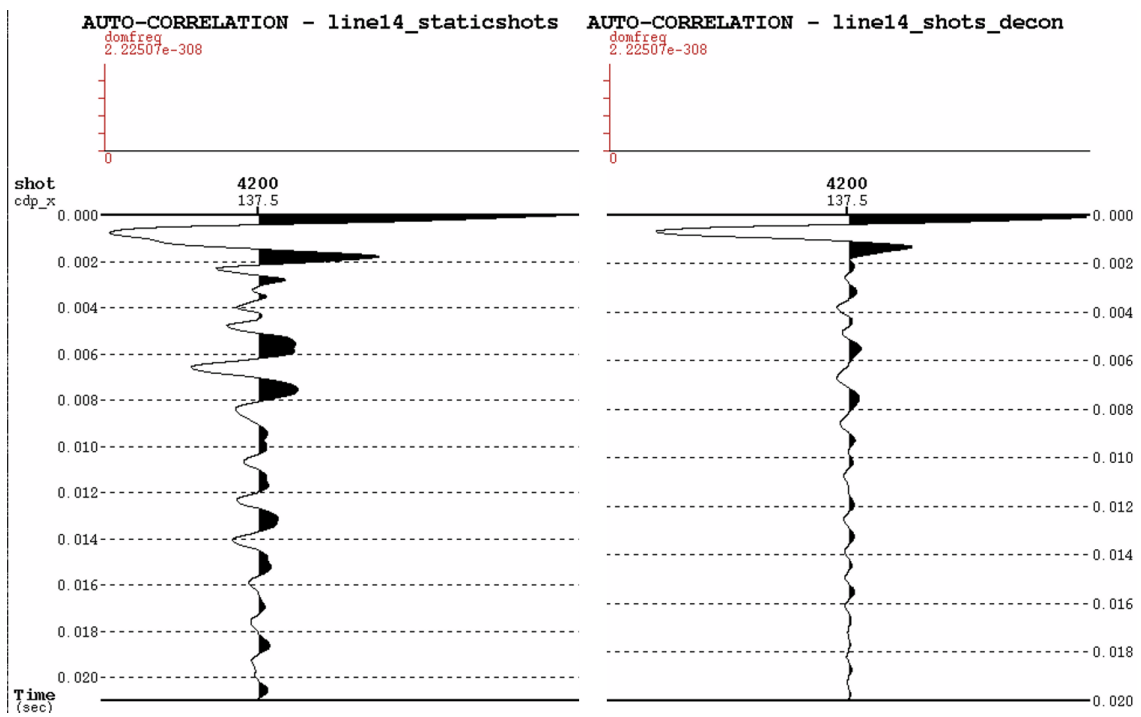
Figure A.5: Auto-correlation of 10 traces in a single shot gather showing the before and after effects of deconvolution. Before deconvolution (left). After deconvolution (right).
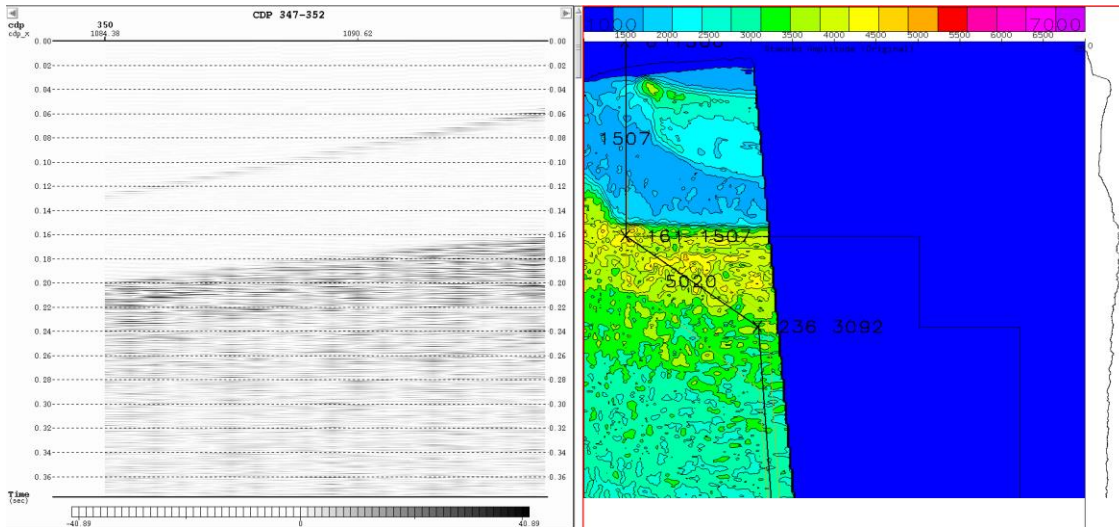
Figure A.6: Interactive velocity analysis window of Paradigm Echos processing software. Variable density of stacked super gather of six CMPs (left). Coherency plot of seismic velocities with picked values (right).
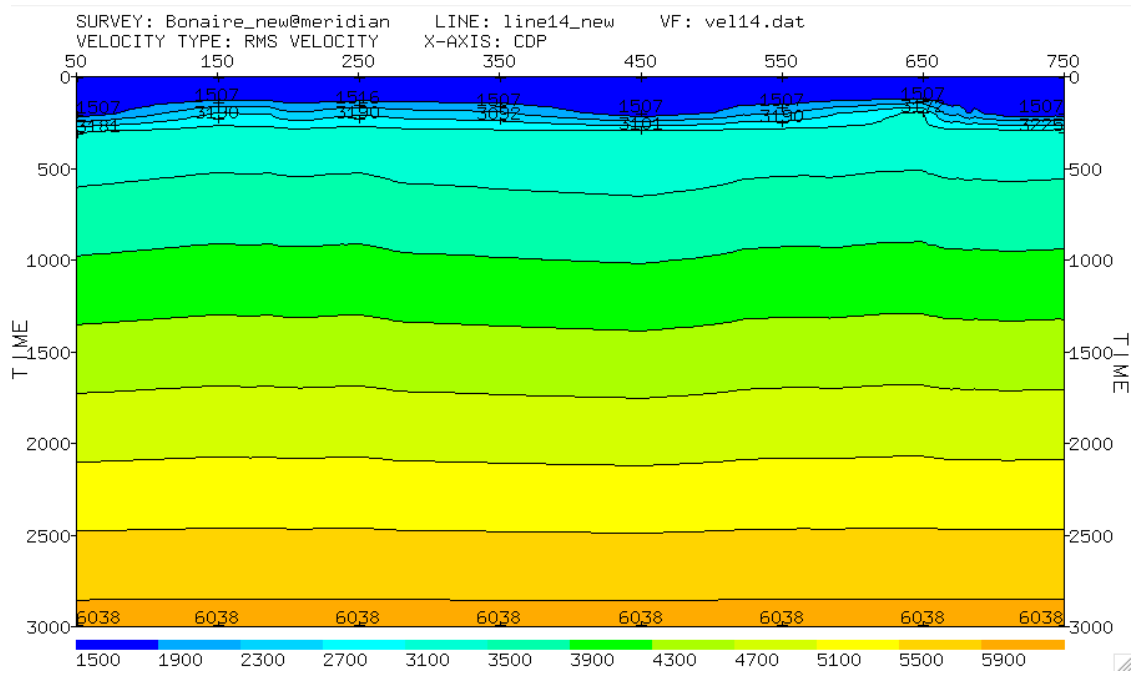
Figure A.7: Root mean square (RMS) velocity model of picked velocities in the velocity database of line 14.
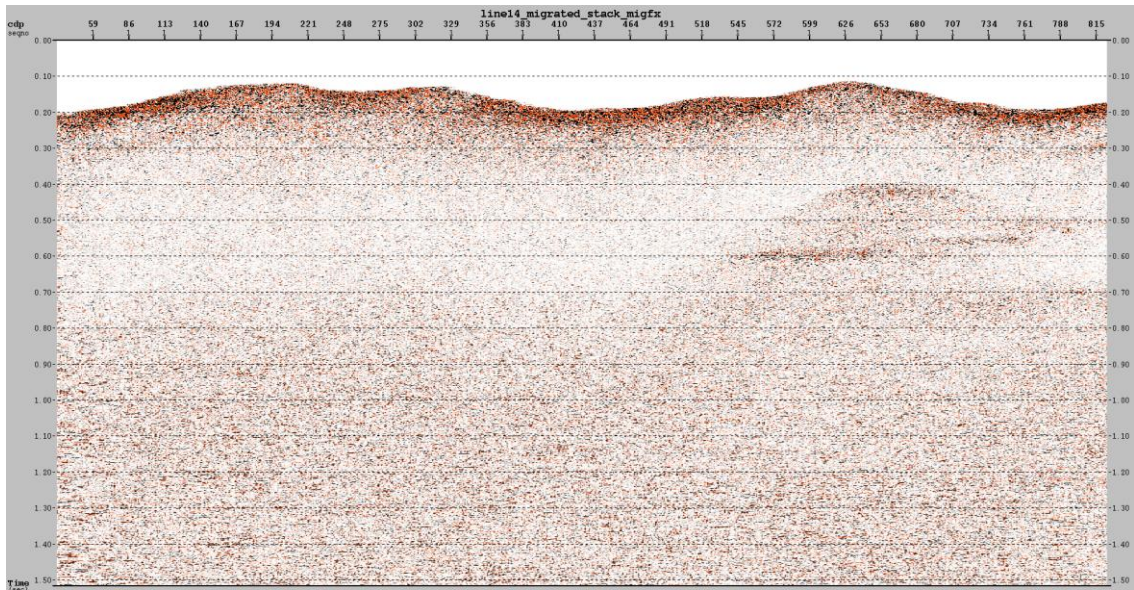
Figure A.8. Stack of line 14 after final processing (NMO, deconvolution, stack, mute, and migration).

Job Name	Input File	Output File
line##_1_geom.dat	NA	NA
line##_2_geomapplystatic.dat	line##_new	line##_staticshots
line##_3_cdpsort.dat	line##_staticshots	line##_cdpsort
line##_4_brutestack.dat	line##_cdpsort	line##_shots_brutestack
line##_5a_decon.dat	line##_staticshots	line##_shots_decon
line##_5b_sort.dat	line##_shots_decon	line##_cdps_decon
line##_6_veldef.dat	line##_cdps_decon	vel##.dat
line##_7_stack.dat	line##_ cdps_decon	line##_stack_post_vel
line##_8_fxmig.dat	line##_stack_post_vel	line##_migrated_stack_migfx

Table A.1: Job name and the file input and output for the respective jobs.